1-14-2021 2:30 PM

Fundamental transport properties in silicon quantum structures

Nazban M. Darukhanawalla, *The University of Western Ontario*

Supervisor: Goncharova, Lyudmila, *The University of Western Ontario*
Co-Supervisor: Simpson, Peter J., *University of British Columbia*
A thesis submitted in partial fulfillment of the requirements for the Master of Science degree in Physics

Abstract

In the field of silicon photonics, there is an effort to bridge the gap between electrical and optical signals on a single platform, creating a need for Si-based light sources. In this project, Si quantum structures – Si quantum wells and quantum dots in SiO_2 were fabricated via solid state precipitation methods. Their properties were studied using X-ray photoelectron spectroscopy, photoluminescence and I-V measurements. Rutherford backscattering spectroscopy was used for depth analysis in monitoring the Si distribution. Different electrical transport mechanisms were explored to understand how an ensemble of silicon QD's or a silicon quantum well behaves in an SiO_2 matrix, with conduction via oxide tunneling and hopping effects. Additionally, we quantified the defect density in epitaxially-grown Si and Ge thin films via RBS channeling, and correlated it with the Debye Temperature measured via low energy electron diffraction to assess the potential use of LEED as a technique for defect analysis.

Keywords

Semiconductors, nanomaterials, quantum dots, quantum well, charge, electrical transport, photoluminescence, Fowler-Nordheim, Poole-Frenkel, defects, Debye Temperature, Rutherford backscattering spectroscopy, photoluminescence, electrical measurements, X-ray photoelectron spectroscopy, low energy electron diffraction, silicon, germanium

Summary for Lay Audience

Conventional computers work via short-range electrical signals sent through silicon-based transistors while long distance communications primarily make use of optic fiber connections, allowing for faster communications and a much greater bandwidth. Silicon quantum dots are a known emitter of light in the near infra-red and visible range of wavelengths and while their optical characteristics are well understood, their electrical characteristics are less well documented. In this thesis, the electrical properties of silicon quantum structures were studied. A variety of experiments were done to create quantum structures within an insulating layer and then probed the sample composition and electrical and optical characteristics. Results were compared with models explaining how these quantum structures affect the characteristics of the sample. Additionally, two independent surface analysis techniques were used to probe defect structures in crystals of silicon and germanium. The results allowed us to verify a new research method for a widely used surface characterization technique. This work will enable our industrial collaborator to probe defects of these crystals during their fabrication process.

Co-Authorship Statement

Chapter 4 of this thesis titled “Surface Debye temperature as a probe for epitaxial thin film defects” was a collaborative effort by Matheus Adam, Lyudmila Goncharova from the University of Western Ontario and Jozef Ociepa, Dan Wells, Bart Checinski, Guen O’Hara and Paige Harford from OCI Vacuum Microengineering Inc., based in London, Ontario. The Rutherford backscattering measurements were performed by members of the University of Western Ontario while low energy electron diffraction measurements were taken by OCI Vacuum.

Acknowledgments

This thesis and all incorporated studies were made possible by the efforts of my supervisors Dr. Lyudmila Goncharova and Dr. Peter Simpson, who have supported me throughout my journey as their student. To Jack Hendriks, for running the Tandetron accelerator that was integral to these studies. Also, a special thanks to Matheus Adam, who was always there to help and give advice. To Tristan Mills, who found the time to help proofread my writing while working on his own research deadlines. To Carolyn Elliott, my fiancée, for when we worked in the same room during the COVID-19 lockdown and she had to listen to my constant talking and yelling whether it be a class I taught, presentation I gave or game I was playing and for supporting me at my lowest and highest points. And to my family, my parents and my brother, who have always stood by me with every decision I make. The truth is I would not be able to do this without support from many more people. Students in the Physics department at UWO who helped me stay sane, the custodian staff who took care of our spaces and to everyone who I interacted with during my time at the University of Western Ontario, thank you. And finally, to the person who is reading this and will (hopefully) find use of this study, this is obviously written for you.

Table of Contents

List of Abbreviations and Symbols

a-	Amorphous-
a_{ex}	Bohr Exciton Radius
BE (EB)	Binding Energy
BLCM	Bulk-Limited Conduction Mechanisms
c-	Crystalline-
CB	Conduction Band
CBM	Conduction Band Minimum
CLB	Coulomb Blocking
D	Confinement Diameter
DFT	Density Functional Theory
DOS (N_c)	Density Of States
DPA	Displacement per Atom
e	Electron
E_g	Bandgap
ELCM	Electrode-Limited Conduction Mechanisms
FN	Fowler-Nordheim
FWHM	Full Width Half Max
h	Hole
HOMO	Highest Occupied Molecular Orbital

LCAO	Linear Combination Of Atomic Orbitals
LEED	Low Energy Electron Diffraction
LUMO	Lowest Unoccupied Molecular Orbital
MBE	Molecular Beam Epitaxy
MEISwin	Medium Energy Ion Scattering Window
MIS	Metal Insulator Semiconductor
MOS	Metal Oxide Semiconductor
MOSFET	Metal Oxide Semiconductor Field Effect Transistor
NCs	Nanocrystals
NIR	Near Infra-Red Wavelengths
PAS	Positron Annihilation Spectroscopy
PF	Poole-Frenkel
PKA	Primary Knock-on Atom
PL	Photoluminescence
PMT	Photomultiplier Tube
Q-Wire	Quantum Wire
QC	Quantum Confinement
QD	Quantum Dot
QW	Quantum Well
Rp	Projected range

RBS	Rutherford backscattering spectroscopy
SEM	Scanning Electron Microscopy
SIMNRA	Simulation for the Analysis of NRA, RBS and ERDA
SoC	System on a Chip
SRIM	Stopping and Range of Ions In Matter
V_O	Oxygen vacancy
VB	Valence Band
VBM	Valence Band Maximum
XAS	X-Ray absorption spectroscopy
XPS	X-Ray photoemission spectroscopy
XRD	X-Ray Diffraction
μ	Electronic/carrier mobility
m_T^*	Tunneling effective mass
v	Frequency of thermal vibrations of electrons
$\hbar$	Planks constant
θ_D	Debye Temperature
ϕ	Barrier Height

List of Tables

List of Figures

List of Appendices

Chapter 1

1. Introduction

Silicon microelectronics have been a staple of human technology for the past seven decades. Electronics with silicon-based components are prevalent in most households and commercial settings across the globe with revenue from the semiconductor industry being 515.51 billion USD in 2019 [1]. Fiber optic communications were developed in the late 1970s and saw a rise in applications with the development of the GaAs semiconductor lasers. Optic cables are used for long distance communication across continents, with cables set deep in the Atlantic and Pacific oceans that can manage nearly 100Gbit/s transmission rate for a single channel [2]. While there are ways to convert from optical to electrical signal and vice versa, the process of conversion can be a bottleneck in transmission rates. In this thesis we look at a subset of nanomaterials that can be used for both optical and electrical transmission and gain an understanding of the transfer processes involved in these materials, to help develop future devices that can potentially convert optical and electrical signal on a single board and push other technologies that combine optical and electrical signals, such as the SoC (System on Chip).

1.1. Photoluminescence of Quantum Dots

1.1.1. Introduction to Quantum Dots

Nanomaterials is a class of materials with any dimensions in the nanoscale or having an internal structure in the nanoscale. Nanomaterials allow us to take advantage of many quantum phenomena, while still maintaining some of the bulk properties. Semiconductor quantum dots (QD) are an example of nanomaterials that are of immense interest in the field of semiconductors and nanotechnology. They are comprised of tiny (typically <10nm) semiconductor nanocrystals that are small enough for their properties to be governed by quantum confinement effects [3]. As the physical size of quantum dots begin to approach a limit of the Bohr exciton radius, quantum mechanical effects gradually begin to dominate certain bulk-physics effects in relation to the QD. In this thesis, we will be looking at the changes in the electrical properties of a material that contains quantum structures (such as quantum wells and quantum dots). We have two possible carriers of electrical charge in semiconductors: the electron (negatively charged) and the hole

(absence of electron, positively charged). While a pure neutral semiconductor (intrinsic semiconductor) may not have many of these free electrons or holes present, we can introduce them into the host material through doping. Doping is the addition of impurity atoms into the system resulting in modifications/addition of band gap levels, thereby changing the electrical and other physical properties of the semiconductor. If we introduce an element containing more valence electrons, we will have a n-doped material that would have electrons being the majority carrier. The opposite of this being the introduction of an element containing fewer valence electrons, creating a p-doped material that would have holes being the majority carrier.

1.1.2. The Exciton

The electron and the hole can also be bound by electrostatic Coulomb forces and this entire system could be mobile within the material, moving energy without a net transfer of charge [4]. This is known as an exciton or electron-hole pair. Excitons are typically created through photon absorption where the photon energy is higher than the bandgap of the semiconductor [5, 6]. This absorption process causes an electron to move from the valence band (VB), also known in chemistry as the highest occupied molecular orbital (HOMO), to conduction band (CB), also known as the lowest unoccupied molecular orbital (LUMO), leaving a hole in the valence band. In general, excitons rapidly dissociate in bulk semiconductor materials. The Bohr exciton radius, a_{ex}, can be defined as the radius for which the orbital angular momentum of the electron-hole pair is an integer of $\hbar$ [3]. We can say that the only force involved is the electrostatic force and hence can write that [6]

$$a_{ex} = \frac{4\pi\varepsilon\,\hbar^2}{m^* e^2} \tag{1.1}$$

where m^* is the effective mass of the electron, hole or exciton and ε is the dielectric constant of the material. π, $\hbar$ & e are all fundamental or mathematical constants ($\pi=3.1416$, $\hbar=1.054\times10^{-34}$ J.s, $e=1.602\times10^{-19}$ C). If the size of the semiconductor nanocrystal becomes smaller than the Bohr exciton radius in any dimension, quantum confinement effects begin to take place. This leads to a raise in energy of the charge carriers and to the changes in physical, electrical and optical properties of the material, making them dependent on the semiconductor nanocrystal size. At confinement sizes, the electron-hole pair (exciton) can be stabilized with resonance forces of

the electron and hole wavefunction overlapping while spatially confined, causing high efficiency of light emission [5].

1.1.3. Bandgap Control – Quantum Confinement

Quantum confinement can be defined as a modification of the free particle dispersion relation dependent on the spatial dimensions of the system. When quantum confinement potential barriers are introduced, we can control the bandgap energy of the quantum dot by changing the QD size & dimension. Moreover, the energy of emitted light photons will be directly depended by the bandgap energy of the system (E_g) and hence the size. By following the particle in a box model and using effective masses from the density of states [3], it has been shown that the bandgap of a quantum structure undergoing quantum confinement can be roughly modeled by equation 1.2 [6]

$$E_{gap}(D) = E_{gap}(\infty) + \frac{A}{D^2} eV.nm^2 \tag{1.2}$$

where E_{gap} (∞) is the bulk material bandgap, D is either the diameter of a spherical quantum dot (QD), the thickness of a quantum well (QW) or diameter of a quantum wire (Qwire), and A is a constant that is calculated based on the confinement type (strong, medium, weak) as calculated by perturbative mass theory [6]. Changing the dimensions of nanomaterials correspondingly changes the confinement properties due to the different degrees of freedom in k space shown via the density of states. For reference, the bulk bandgap for crystalline Si is 1.11eV at 300K [7] corresponding to light emission at ~1120nm. While Si-QD systems can have $E_g > 2.0$ eV, corresponding to emission wavelength of around 600nm.

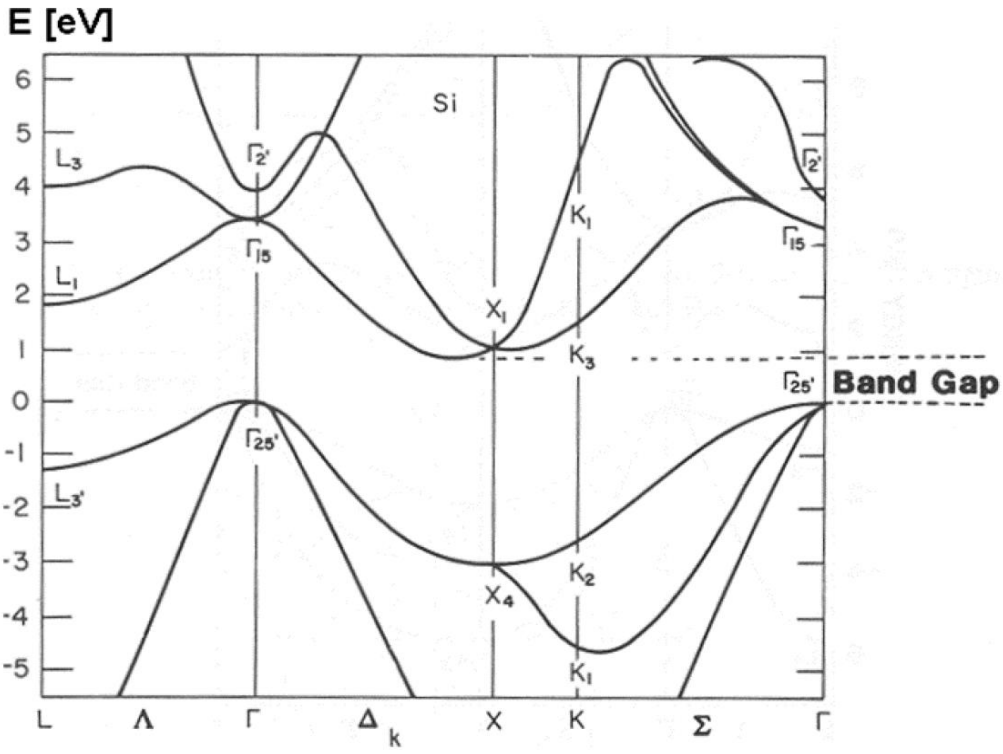

Figure 1.1: Band structure of silicon in the wavevector (k-space). Specified region at approximately 0 eV showcases the forbidden region – bandgap of Si to be around 1.11eV.

1.1.4. Recombinations: The band structure of silicon

Now that we see how the bandgap energy can be controlled by size of a semiconductor QS, we need to see how the band structure of silicon becomes relevant in this thesis. When an exciton relaxes, the electron goes down from the conduction band (CB) to valence band (VB) in a process known as recombination. The bandgap controls the emission energy (and corresponding wavelength/frequency) from the system. In optical transitions, both energy and momentum must be conserved, this means that for a given transition, both an energy component (photon) and momentum component (phonon) should be considered. In cases where there are no changes in the momentum of a transition (no phonon involved), the bandgap is said to be direct. For indirect semiconductors, one needs a change in momentum space (via an absorption or emission of a phonon) to achieve radiation recombination. When photons are emitted (regardless of bandgap type), the process is known as radiative recombination.

Looking at the energy band structure of silicon in Figure 1.1, the k (momentum) vector is different for the conduction band minimum (X) and valence band maximum (Γ) points. This shows that silicon has an indirect bandgap, and hence radiative recombination's both photons and phonons are involved. Indirect bandgap materials are known to have very inefficient recombination process with long radiative lifetimes on the order of milliseconds [8]. Although, in general, radiative lifetimes are heavily influenced not just by the bandgap type but the size of the quantum dot themselves [9].

Direct bandgaps semiconductors, such as InAs, GaAs, CdTe, are efficient light emitters. On an opposite side, in cases where the charge carriers recombine via releasing a phonon, the process is known as nonradiative recombination. This is usually considered a waste of energy for photonic and optoelectronic applications, as the primary goal is to maximize photon emission.

1.2. Electrical Properties of Metal Insulator Semiconductor (MIS) Interface

The samples in this thesis consist of an ensemble of QDs embedded in an insulating matrix or ultra-thin Si films (quantum wells, QW) between insulating SiO_2 layers. Systems like these can be defined and modeled as Metal Insulator Semiconductor (where the insulator is usually an oxide, called Metal Oxide Semiconductor or MOS) structures with Al contact pads as the metal, SiO_2 as the insulator and the Si QD as the semiconductor. When measuring current voltage (I-V) curves, resistance across the MOS structure dominates over resistance via conduction between quantum dots. Hence, we essentially study the system as a whole and see how MOS structures with embedded quantum structures transport charges.

1.2.1. Charge Carriers in the MIS system

A lot of the earlier overview papers on conduction through thin dielectric films can be traced back/towards J.G. Simmons of the University of Toronto. From the late 60's to early 70's, he developed papers detailing conduction through dielectric films <1-2μm thick (with corresponding *E* fields being around 10^4-10^5 V cm^{-1}) [10].

Simmons believed that extrinsic carriers and defects played a major role in the conduction mechanisms of dielectric films. SiO_2 is described to conduct via Si_2 (Si-Si chains), SiO and SiO_2

alongside free Si or vacancies in the film. Impurities can also affect these conductive pathways, and much care must be taken to ensure that the impurity count is kept to a minimum.

One of Simmons' models involves tunneling through a trapezoidal barrier [11]. The corresponding equation is for $0 < V \leq \phi/e$, where ϕ is the barrier height between the metal and semiconductor. And at relatively low voltages, reduces to the form [11]

$$I = \theta(V + \gamma V^3) \tag{1.3}$$

where the model terms are

$$\theta = \left(\frac{e}{h}\right)^2 \frac{[m(\Phi_1 + \Phi_2)]^{1/2}}{s} exp\left[-D\left(\frac{\Phi_1 + \Phi_2}{2}\right)^{1/2}\right] \tag{1.4}$$

$$\gamma = \frac{(De)^2}{[48\,(\Phi_1 + \Phi_2)]} - \frac{De^2}{32}\left[\frac{2}{(\Phi_1 + \Phi_2)}\right]^{3/2} \tag{1.5}$$

$$D = \frac{\left[4\pi s(2m)^{1/2}\right]}{h} \tag{1.6}$$

Where s is the thickness of the dielectric, Φ_1 is the barrier height at the first electrode – dielectric interface, Φ_2 is the barrier height at the second electrode – dielectric interface, m and e are the electron mass and charge, respectively. At the high E-field limit ($V >> \Delta\Phi$), these equations get reduced to a Fowler-Nordheim model [10, 11], which is discussed in the next section.

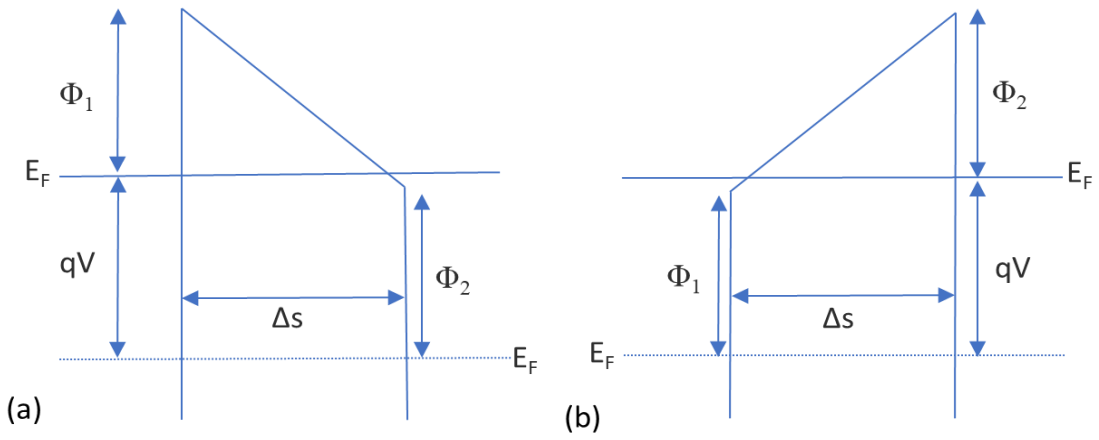

Figure 1.2: Energy diagram of barrier between dissimilar electrodes at different (high field) potential, with (a) electrodes reverse biased and (b) electrodes forward biased.

1.2.2. Conventional Transport Models

For mechanisms of metal insulator semiconductor (MIS) interfaces, different charge transport mechanisms can be identified depending on (a) temperature, (b) electric field, and (c) other external factors. In general, conduction mechanisms are routinely split into two categories. The first being electrode-limited conduction mechanisms (ELCM) where the electrical properties at the electrode-dielectric interface control the mechanism. Properties such as barrier height and carrier effective mass are of importance here. And the second being bulk-limited conduction mechanisms (BLCM), which are dependant on the properties of the dielectric itself. Factors such as trap level, trap spacing and density, carrier drift mobility, dielectric relaxation time and density of states in conduction band affect BLCM.

Electrode-Limited Conduction Mechanisms

Schottky conduction (modified thermionic emission)

In both Schottky and thermionic emission, the electrons obtain enough energy through thermal activation to overcome the potential barrier in the MIS interface. The Schottky bias lowers metal-insulator interface barrier height and allows for electron emission through the metal-insulator interface [12]. Schottky model assumes that the image force is limited to a distance x_o of the electron from the surface of electrode. The potential barrier is lowered under the influence of an electric field, due to the interaction of the field with the image force. The expression for

Schottky emission (trap-limited, when the electronic mean free path is less than the dielectric thickness ($l < t_d$) is written as:

$$J = \alpha T^{3/2} E\mu \left(\frac{m^*}{m_0}\right)^{3/2} exp\left[\frac{-q\left(\Phi_B - \sqrt{qE/4\pi\epsilon_r \epsilon_0}\right)}{kT}\right] \quad (1.7)$$

where $\alpha = 3\times10^{-4}$ A s cm^{-3} K$^{-3/2}$, m^* is the effective mass, μ is the electronic mobility in the insulator and $q\Phi_b$ is the Schottky barrier height (conduction band offset) which can be calculated for a known system of varying thicknesses. Equation (1.7) shows that in the Schottky model, the current density, J, A/cm^2 has an exponential dependence on the square root of the applied field. Therefore, the plot of ln (J/E) versus $(E)^{1/2}$ should give a linear fit, with the slope presenting the Schottky barrier height at a fixed temperature.

Fowler-Nordheim Tunneling (FNT)

In the classical setting, the energy of incident electrons is lower than the potential barrier height, the electrons would be reflected. However, in quantum mechanics, we know that the electron wavefunction can penetrate the barrier when it is sufficiently thin (<100Å). Fowler-Nordheim tunneling is the calculation model for the current that can go through the barrier for a corresponding applied electric field. FN can be singled out as the dominating mechanisms for thicker oxides (>5nm) at low temperatures (<100K) where thermionic emissions are greatly reduced. The probability of an electron to penetrate from one electrode to the other side through the insulator is strongly dependent on the applied electric field. Quantitatively the current density can be expressed by equation (1.8), which shows that the tunnel current will be affected by electron effective mass (m_T^*), barrier height of the semiconductor-oxide interface (Φ_b) and shape of the potential:

$$J = \left(\frac{q^3E^2}{8\pi hq\Phi_b}\right) exp\left[\frac{-8(2qm_T^*)}{3hE}\Phi_b^{3/2}\right] \quad (1.8)$$

Additionally, we can denote that a plot of *log* (J/E^2) against ($1/E$) should give a straight line. The slope of this representation, commonly called a Fowler-Nordheim (FN) plot allow us to experimentally estimate the barrier height of a material [13].

$$slope = -6.83 \times 10^7 \sqrt{\left(\frac{m_T^*}{m_0}\right) \Phi_b^3} \left(\frac{cm}{V}\right) \quad (1.9)$$

Bulk-Limited Conduction Mechanisms

Poole-Frenkel emission

Like Schottky, Poole-Frenkel (PF) emission occurs due to thermal excitation of electrons going over the metal-insulator barrier. However, PF emission occurs via trap sites (defects in the crystalline matrix) to the conduction band of the insulator. The Coulomb potential energy of the electron is reduced by the applied electrical field across the insulator interface. This reduction in energy increases the probability of an electron getting thermally excited out of the trap and can be modeled as a modification of Schottky emission.

$$J = q\mu N_c E \ exp\left[\frac{-q\left(\Phi_T - \sqrt{qE/4\pi\epsilon_r\epsilon_0}\right)}{2kT}\right] \quad (1.10)$$

where μ is the electronic drift mobility, N_c is the effective density of states in the conduction band and Φ_T is the trap energy level. It should be noted that the 2 in the exponential denominator is included in the model only when the number of trap centers are on the same order as donor centers ($N_d \approx N_t$) and is known as the modified/anomalous Poole-Frenkel emission. Since this is a modification to Schottky/thermionic emission, we expect to see high PF emissions at high temperatures and electric fields and can only be further distinguished from Schottky emission using other system parameters. Previous studies have observed PF onset at around room temperature [14]. In measuring the slope of PF emissions, the optical dielectric constant ε_r can be determined. Since electron emissions take place on a much shorter timescale than the dielectric relaxation time, the orientation polarization is unable to react in time and the optical dielectric is left to be the dominating dielectric constant.

With an increase in *E* field, the potential barrier at the far side of the trap decreases and the electron can easily escape from the trap into the dielectric. There will be a saturation limit at

$$\Phi_T = \sqrt{qE/4\pi\epsilon_r\epsilon_0} \quad (1.11)$$

where all traps are ionized due to their barrier height being decreased to the ground state of the trap. At this saturation limit the current density can be defined as

$$J = q\mu N_c E \quad (1.12)$$

which is independent of temperature. Hence PF emission plots taken at different temperatures should all have the same saturation current dependant only on the terms in Equation (1.12).

Hopping conduction

Hopping conduction can be seen when electrons tunnel from one trap site to another within the insulator itself. Unlike PF emission which occurs due to thermionic excitation of electrons being able to overcome the barrier, the electron/carrier energy is lower than the potential barrier and hopping conduction occurs due to tunneling (like FN tunneling) effects between trap sites within the conduction band of the insulator. It can be modeled the following way: [15]

$$J = qanv\ exp\left[\frac{qa_tE}{kT} - \frac{E_a}{kT}\right] \quad (1.13)$$

where a_t is the mean distance between trap sites, n is the electron concentration in the conduction band of the insulator, v is the frequency of thermal vibrations of electrons within trap sites and E_a is the activation energy (the energy level from trap states to the conduction band E_c). As an example, hopping conduction has been reported to follow experimental data very well in low electric fields (<0.6MV/cm) in Pr_2O_3 MIS structures and appears to be more evident at lower temperatures (Figure 1.3) [16].

Due to the nature of the samples in this thesis, it is difficult to differentiate trap sites simply as defects in the structure, the quantum dot itself or the defects at the SiQDs-SiO_2 interface. Different sample fabrication procedures are used to ensure variable defect concentrations and to measure differences in conduction mechanisms between them. While modelling defects as quantum dots might be useful, this creates an issue with PL emission since optimizing that would result in an increase in non-radiative recombination.

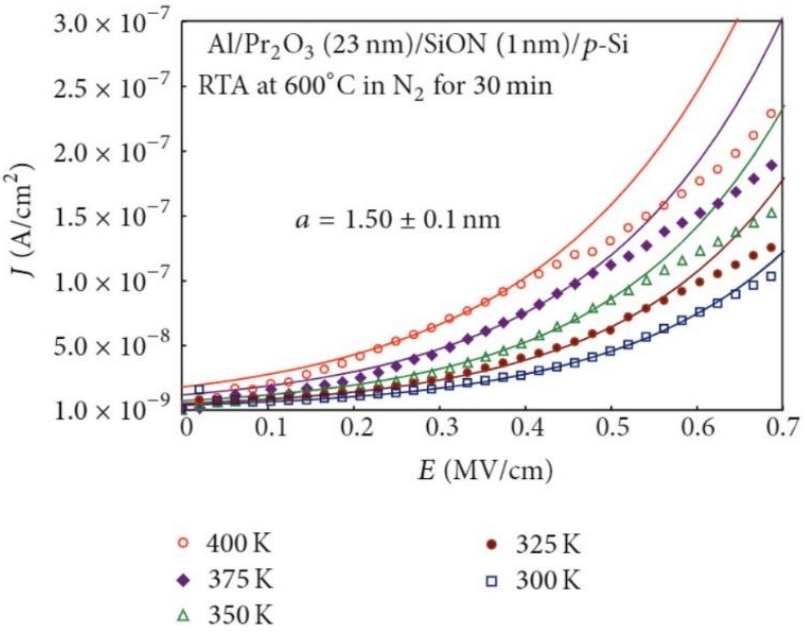

Figure 1.3: *J-E* curves with simulation and experimental data for hopping conduction for laminated Pr_2O_3/SiON MIS capacitors at low electric fields. [12]

Transition from Electrode Limited to Bulk Limited Models

The transition period of the model depends on a multitude of factors including the doping and trap density of the semiconductor. If the depletion region is small enough, the bulk conductivity is low enough for one to observe the transition between conduction processes. Simmons noted that field emission electrons will rapidly increase current with initial applied voltage.

1.3. Conduction properties of Si QDs in SiO_2

1.3.1. Role of SiQDs-SiO_2 interface

Many attempts have been made to understand the electrical and optical properties of quantum dots[17, 18]. Initial research has shown that the interface region between the Si QDs and SiO_2 matrix is not as sharp as once thought but is instead an intermediate region of amorphous nature and variable composition. This region influences light emission and it has been shown that the transition region has a large light emission when x-ray energy is resonant with the SiO_2 absorption edge [17].

Studies have been done to theoretically analyze the electronic and optical properties of both relaxed and strained nanostructures embedded into SiO_2 [19]. Density functional theory (DFT) calculations show that the optical and electronic properties of the Si QD - SiO_2 interface changes drastically based on the strain, termination and amorphization of the embedded NC with the latter being the strongest factor. Higher amorphization leads to a larger redshift of the energy bandgap that scale alongside the size of the quantum dot [20]. This effect has also been seen in an experimental setting [21]. However, there is still debate as to the degree of importance interface defects in radiative recombination of the SiQDs.

While amorphization of the SiQD-SiO_2 interface plays a role in the electrical and optical properties of the system, the coordination of Si and O atoms at the Si/SiO_2 interface play a role in quantum confinement as well [20]. As can be observed in Figure 1.4, there is a correlation between the bandgap of the system and the oxidation degree, showing evidence that the co-ordination number of oxygen atoms in the Si QD-SiO_2 interface region greatly influence quantum confinement and the corresponding bandgap size. This has been experimentally observed with shifting of XPS spectra Si-2p orbital in a size dependent study where the suboxide states Si^{1+}, Si^{2+}, Si^{3+} are studied [20].

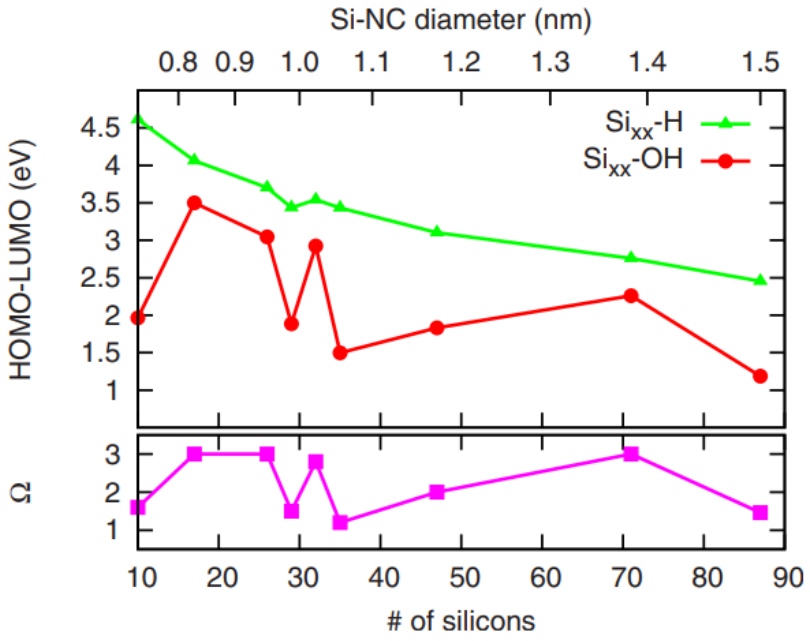

Figure 1.4: Bandgap for the hydroxide and hydrogenated Si quantum dots, together with the oxidation/hydrogenation degree (Ω). [20]

Additionally, at a certain density of embedded QDs, a percolation threshold will be reached where many of the Si-SiO_2 interfaces or QD themselves are in direct contact with each other, which can be thought of as a single layer of QDs in direct contact with each other. These structures allow for much easier conduction through the sample, as the dominating effect of resistance will be from the oxide layer above the sample. Samples with an embedded density of Si quantum structures below this percolation threshold are referred to as quantum dot (QD) samples while those above the threshold are referred to as quantum well (QW) structures in this thesis. Si QDs were formed via ion implantation while Si QW structures were formed via molecular beam epitaxy.

1.3.2. Coulomb blocking effects

Much effort has been given in trying to bridge the gap between theory models and experimental data in understanding the transport mechanisms of an ensemble of Si-QDs in an oxide matrix. Most approximations do not consider QD-QD interactions, implying an inter QD distance of ~0.5nm [22] which can be filled with low Si QD concentrations in fabrication processes. A large Stokes shift has been observed in light emission spectra by several independent researchers and has been attributed to amorphization and oxidation states in the SiQD-SiO_2 interface and tunneling between Si QDs. While it is hard to experimentally differentiate the weight of each factor above, attempts have been made.

Another observed effect in QD systems is the coulomb blocking effect (CLB). Originally observed in single electron charging systems [23, 24], the coulomb blocking effect is observed when a single electron penetrates the barrier and creates strong coulomb repulsion the prevents other electrons from flowing through the system (Figure 1.5) [25]. It gets overcome at specific intervals of electric field that are related to the capacitance of the quantum dot system. This capacitance is modelled as

$$C = 4\pi\epsilon_r r\left[1 + \frac{r}{2l} + \frac{\left(\frac{r}{2l}\right)^2}{1 - \left(\frac{r}{2l}\right)^2}\right] \tag{1.14}$$

which allows us to define $\Delta V = e^2/C$. Conventionally, this effect is measured when $e^2/2C >> kT$, implying that the electrostatic charging dominates thermal energy. For 1.5nm to 5nm quantum

dot sizes, the energy ranges are 180meV to 32meV respectively, which is still higher than kT of 25.8meV at room temperature. Hence for quantum dots that are 5nm or smaller, we should still be able to measure coulomb blocking effects at room temperature.

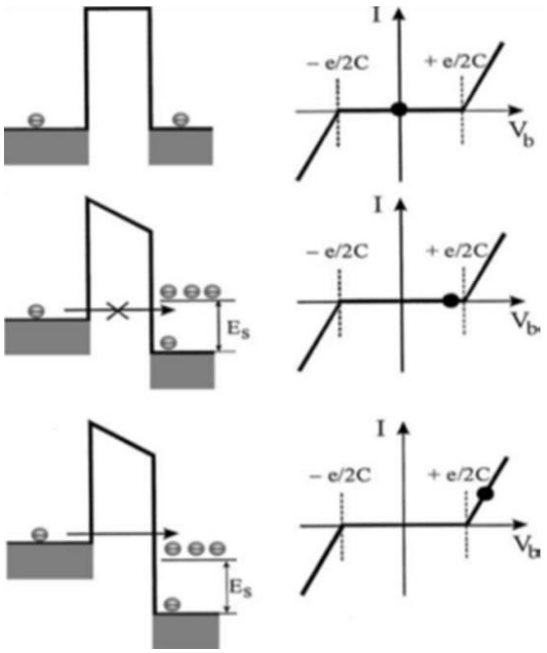

Figure 1.5: Illustration of Coulomb blockade in a thin junction with a small capacitance (~ aF). a) $V_b = 0$: there is no electron tunneling through the barrier. b) $e|V_b| < E_s$: There is no electron tunneling. c) $E_s < e|V_b|$: Electron flow occurs.

1.4. Debye Temperature and defect characterization

Following the idea that defects are important in charge transport of quantum dots, it is prudent to understand the defects in a more quantitative way and find a way to better monitor them for use in industrial applications. Defects in substrates can be monitored in many different ways. Defects at the surface and bulk material (~1-5 μm) can be observed using RBS (Rutherford Backscattering Spectrometry) while the surface can be more accurately probed with LEED (Low Energy Electron Diffraction).

The Debye model estimates phonon contribution to the specific heat of a material; within this model the Debye temperature (θ_D) is a parameter that defines the highest temperature that can be achieved due to normal mode of lattice vibrations. Studies have shown the effect of the Debye

temperature on vacancy clusters (hence electrical conductivity) [26, 27]. An analytical relationship between Debye temperature and bandgap was found to be [27]

$$T_D = T_0 \exp\left(\gamma \frac{E_g}{2kT}\right) \tag{1.15}$$

with a numeric constant γ chosen to fit the data, this model can be confirmed by fitting it to known values of E_g and T_D of different semiconductor materials (Figure 1.6). Defects have already been shown to influence the thermoelectric properties and bandgap of materials, hence changing the Debye temperature. Some studies have already calculated the Debye temperature in bulk materials to be

$$\theta_D(T) = T\left[\frac{9Nk}{C_v^D}\int_0^{\theta_D/T} \frac{x^4 e^x}{(e^x-1)^2}\,dx\right]^{1/3} \tag{1.16}$$

where N is the number of atoms per unit cell and C_v^D is the actual heat capacity. For reference the Debye Temperatures of bulk Si and Ge are 640K and 374K respectively [28].

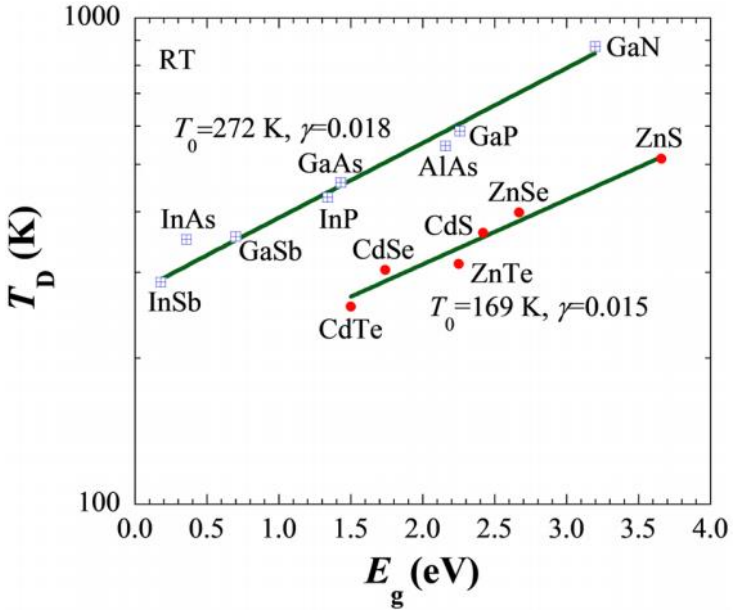

Figure 1.6: The plot of Debye temperature T_D vs. E_g for the III-V and II-VI compound semiconductors (bulk). The solid lines are fits done with Eq.(1.17) [27]

Via LEED measurements, the Debye Temperature can be calculated using a set of equations which connects the Debye-Waller Factor (W), Debye Temperature θ_D, and the scattering intensity of an electron beam incident on a crystal (I):

$$2W = \frac{24m_e(Ecos^2\alpha + V_0)T}{m_a k(\theta_D)^2} \tag{1.17}$$

$$I - I_{bk} = I_0 e^{-2W} \tag{1.18}$$

which can be rearranged to

$$\ln\frac{I - I_{bk}}{I_0} = -\frac{24m_e(Ecos^2\alpha + V_0)}{m_a k(\theta_D)^2}T \tag{1.19}$$

Where a plot of intensity vs temperature would give us a slope from which the Debye temperature can be calculated.

1.5. Thesis Format and Research Contribution

Chapter 1 has detailed the literature and past research that relates to the work done in this thesis. Chapter 2 will focus on the methodology and experimental details of the experiments that were done in making this thesis. As this is an integrated article thesis, chapter 3 focuses on the study of transport mechanisms of Si quantum structures in an SiO_2 matrix, detailing their depth profiles, optical and electrical characteristics. Chapter 4 will discuss a project done with collaborators at OCI-Vacuum, a company that specializes in designing and manufacturing equipment for low energy electron diffraction (LEED) measurements. The defect measurement capabilities of LEED (via the Debye temperature) and RBS are compared.

My efforts in this thesis were in the research and designing of the implanted Si-QDs in SiO_2 and in all of the experiments that were performed in Chapter 3. Jack Hendriks at the Tandetron facility at the University of Western Ontario (UWO) performed the implantation process, while Todd Simpson at the Nanofabrication facility at UWO performed the lithography process in creating Al contact pads. The MBE grown Si samples were created by Aysegul Abdelal during her time as an MSc student at the Goncharova lab. All RBS, optical and electrical measurements in Chapter 3 were performed by me (with Jack Hendriks running the Tandetron accelerator for

RBS measurements) and any figures shown in Chapters 3 were fully designed by me unless specified otherwise. The electrical measurement setup was designed and built by me (with special help from Dr. Goncharova and Dr. Simpson) in the Goncharova Nanophysics Lab in the University of Western Ontario. RBS experiments in Chapter 4 were performed by both Matheus Adam (PhD candidate) and I, with LEED measurements being performed by our collaborators at OCI Vacuum.

1.6. References

[1] W. Chou, Semiconductors – the Next Wave Opportunities and winning strategies for semiconductor companies in: Deloitte (Ed.), 2019.

[2] F. Poletti, N. Wheeler, M. Petrovich, N. Baddela, E.N. Fokoua, J. Hayes, D. Gray, Z. Li, R. Slavík, D. Richardson, Towards high-capacity fibre-optic communications at the speed of light in vacuum, Nature Photonics, 7 (2013) 279-284.

[3] E.G. Barbagiovanni, D.J. Lockwood, P.J. Simpson, L.V. Goncharova, Quantum confinement in Si and Ge nanostructures: theory and experiment., Applied Physics Reviews, DOI (2014) 1(1), 011302.

[4] V. Agranovich, Excitations in Organic Solids, Oxford Scholarship Online, 2008.

[5] A.M. Smith, S. Nie, Semiconductor nanocrystals: structure, properties, and band gap engineering., Accounts of chemical research, DOI (2009) 43(42), 190-200.

[6] E.G. Barbagiovanni, D.J. Lockwood, P.J. Simpson, L.V. Goncharova, Quantum confinement in Si and Ge nanostructures, Journal of Applied Physics, DOI (2012) 111(113), 034307.

[7] C. Kittel, Introduction to Solid State Physics, New York: John Wiley, 1986, pp. 185.

[8] L. Goncharova, P. Nguyen, V. Karner, R. D'Ortenzio, S. Chaudhary, C. Mokry, P. Simpson, Si quantum dots in silicon nitride: Quantum confinement and defects, Journal of Applied Physics, 118 (2015) 224302.

[9] T. Takagahara, K. Takeda, Theory of the quantum confinement effect on excitons in quantum dots of indirect-gap materials, Physical Review B, 46 (1992) 15578.

[10] J.G. Simmons, Conduction in thin dielectric films, Journal of Physics D: Applied Physics, 4 (1971) 613-657.

[11] J.G. Simmons, Electric Tunnel Effect between Dissimilar Electrodes Separated by a Thin Insulating Film, Journal of Applied Physics, 34 (1963) 2581-2590.

[12] F.C. Chiu, A review on conduction mechanisms in dielectric films, Advances in Materials Science and Engineering, 2014 (2014).

[13] D.K. Schroder, Semiconductor Material and Device Characterizationedition, John Wiley & Sons, New York, 1998.

[14] Q.F. Pan, Q. Liu, Poole–Frenkel Emission Saturation and Its Effects on Time-to-Failure in Ta-Ta_2O_5-MnO_2 Capacitors, Advances in Materials Science and Engineering, 2019 (2019) 1690378.

[15] N.F. Mott, E.A. Davis, Electronic Processes in Non-Crystalline Materials, Oxford University Press, DOI (1979.).

[16] J.Y.M. Lee, F.C. Chiu, P.C. Juan, T.Y. Tseng, H.S. Nalwa, The application of high-dielectric-constant and ferroelectric thin filmsin integrated circuit technology, Handbook of Nanoceramics and Their Based Nanodevice, 4 (2009).

[17] N. Daldosso, M. Luppi, S. Ossicini, E. Degoli, R. Magri, G. Dalba, P. Fornasini, R. Grisenti, F. Rocca, L. Pavesi, Role of the interface region on the optoelectronic properties of silicon nanocrystals embedded in SiO_2, Physical Review B, 68 (2003) 085327.

[18] M. Luppi, S. Ossicini, Ab initio study on oxidized silicon clusters and silicon nanocrystals embedded in SiO_2: Beyond the quantum confinement effect, Physical Review B, 71 (2005) 035340.

[19] R. Guerra, I. Marri, R. Magri, L. Martin-Samos, O. Pulci, E. Degoli, S. Ossicini, Silicon nanocrystallites in a SiO_2 matrix: Role of disorder and size, Physical Review B, 79 (2009) 155320.

[20] R. Guerra, E. Degoli, S. Ossicini, Size, oxidation, and strain in small Si/SiO_2 nanocrystals, Physical Review B, 80 (2009) 155332.

[21] B. Gallas, I. Stenger, C.C. Kao, S. Fisson, G. Vuye, J. Rivory, Optical properties of Si nanocrystals embedded in SiO_2, Physical Review B, 72 (2005) 155319.

[22] S. Ossicini, M. Govoni, R. Guerra, I. Marri, Silicon nanocrystals for photonics and photovoltaics: Ab initio results, DOI (2016).

[23] D.V. Averin, K.K. Likharev, Coulomb blockade of single-electron tunneling, and coherent oscillations in small tunnel junctions, Journal of Low Temperature Physics, 62 (1986) 345-373.

[24] M.D. Efremov, G.N. Kamaev, V.A. Volodin, S.A. Arzhannikova, G.A. Kachurin, S.G. Cherkova, A.V. Kretinin, V.V. Malyutina-Bronskaya, D.V. Marin, Coulomb blockade of the conductivity of SiO_x films due to one-electron charging of a silicon quantum dot in a chain of electronic states, Semiconductors, 39 (2005) 910-916.

[25] A. Nikniazi, F. Sohrabi, M. Sajadi, The effect of quantum dot size on coulomb blockade in quantum computers, 2013.

[26] P. Huang, C. Lu, Effects of vacancy cluster defects on electrical and thermodynamic properties of silicon crystals, The Scientific World Journal, 2014 (2014).

[27] M. Bhowmick, B. Ullrich, M. Androulidaki, H. Xi, The thermo-electric nature of the Debye temperature, AIP Advances, 8 (2018) 055318.

[28] F. Schaffler, Silicon-Germanium (Si1-xGex), Properties of Advanced Semiconductor Materials GaN, AlN, InN, BN, SiC, SiGe, DOI (2001) 149-188.

Chapter 2

2. Methodology

2.1. Sample Fabrication

Silicon quantum structures can be fabricated in many ways and typically can either be formed in colloidal solutions (with a stabilizing agent to passivate the surface bonds) or embedded in a thin film on silicon wafer (solid state form). In this thesis the focus is solely on the solid state form as the goal is to be as compatible as possible with current semiconductor or optoelectronics industry standards. This group of fabrication methods is based on the low mobility (diffusivity) of Si atoms in SiO_2, leading to Ostwald ripening of Si atoms within the oxide layer, forming nanocrystals or quantum dots. These techniques include, but are not limited to, chemical vapour deposition (CVD), molecular beam epitaxy (MBE) and ion implantation. In the part of the project related to electrical transport in Si quantum structures, two sets of samples were fabricated. The first set was grown by MBE while the second set was prepared by ion implantation. Essential features of both MBE and ion implantation methods are given in the subsections below. Surface preparation steps in the second project, related to surface Debye temperature studies, will be discussed in Chapter 4.

2.1.1. Molecular Beam Epitaxy

As the name suggests, molecular beam epitaxy (MBE) is an epitaxial method by which the single-crystal layer of the film is formed in a well-defined orientation along the crystalline substrate surface. It was first commercially used in the late 1970's at Bell Telephone Laboratories. To this date, MBE is extensively used in the manufacturing of semiconductor devices including transistors, (such as Metal on Oxide Field Effect Transistors MOSFETs) and light emitting diodes used in optical CD and DVD disk readers [1]. While MBE is used in the industry it also allows for the fabrication of nanostructures that allow monolithical integration on Si wafers where multiple circuit elements can be fabricated on the same chip. This reduction of interference allows for increased efficiency and sensitive measurements [2, 3]. With how widespread MBE is in the semiconductor and nanotechnology industry, it is utilized as one of fabrication methods here.

In MBE systems, an atomic beam is formed by an e-beam hitting a solid pure target and then elemental flux is focused onto the single-crystal substrate. Growth can be ordered or disordered depending on several parameters such as flux rate, temperature, vacuum level, substrate surface structure, and lattice mismatch between the substrate and the film [4].

MBE samples were fabricated by Aysegul Abdelal [4] in an MBE chamber (Kurt Lesker) located in the Tandetron Facility at the University of Western Ontario (WSC G49), at 300^{o}C with a deposition rate less than 0.2Å/s. This system is pumped by a cryo-pump to achieve 10^{-7} Pa vacuum environment to ensure minimal contamination at low deposition rates [5]. Scanning electron microscopy (SEM) and atomic force microscopy (AFM) imaging was conducted to characterize topological features for these samples. Results of this imaging are presented here (Figure 2.1) [4] and show no significant evidence of 3D Si islands formation, supporting the idea that our structures are relatively flat ultra-thin films with average roughness of 2-5 nm. After Si layer growth was completed, a 20nm thick SiO_2 layer was grown on top of these samples via Plasma Enhanced Chemical Vapor Deposition (PECVD) at 250^{o}C at the Western Nanofabrication Facility.

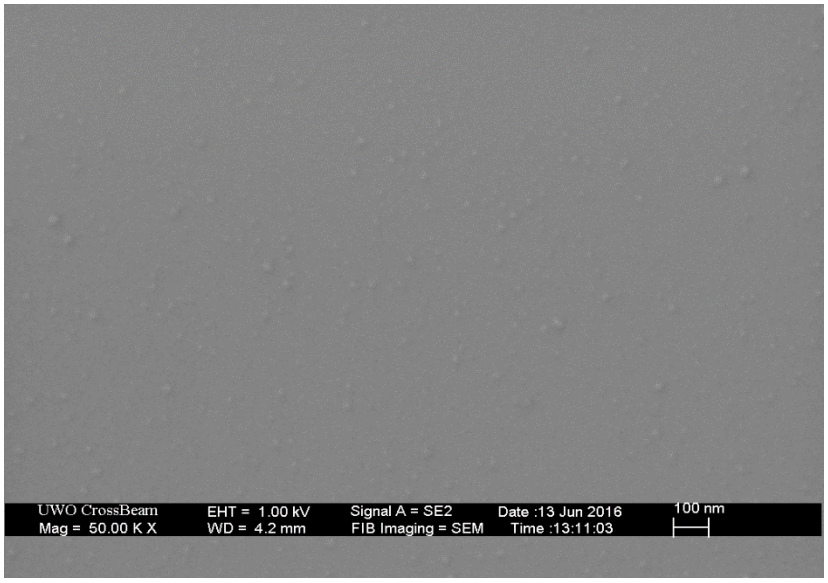

Figure 2.1: SEM Image of MBE Si grown on SiO_2, showing surface roughness after growth.

2.1.2. Ion Implantation Samples

Ion implantation was developed in the mid-1960's for Si doping with selective impurities to form p-n junctions, and other applications [6]. In this process ions are accelerated into the sample at a well-controlled energy in the 5-200keV range and ion dosage. The depth profile is dependent on the energy which not only affects the mean implantation depth, but also the straggling distribution (standard deviation of implants vs depth) (Figure 2.2 (a)), where lower energies give a smaller spread and larger energies have a larger spread.

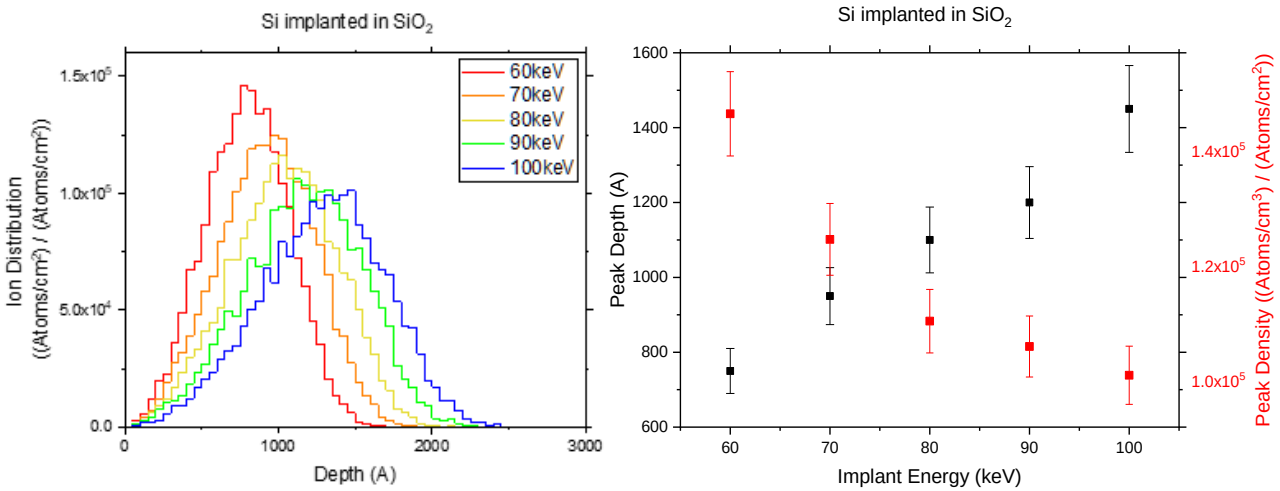

Figure 2.2: (a) Implantation depth profiles of Si implanted into SiO_2 in the 60 to 100keV range. (b) Summary figure shows the peak depth increasing and the peak density decreasing respectively with energy.

The dosage is simply the total charge of ions implanted and hence controls the density of ions (at/cm^3) that are implanted into the system. Low dosages are usually used to dope the material, while higher dosages (beyond a supersaturation limit, typically followed by a high temperature thermal treatment) may cause the implanted material to nucleate into crystals and form a continuous layer. Simulations of ion implantations are made using SRIM (Stopping Range of Ions in Matter) [7], a Monte-Carlo simulation of interactions between ions and target substrates written by James F. Ziegler and Jochen P. Biersack.

A typical SRIM-simulated Si and vacancy depth profile is shown below in Figure 2.4 which presents the ion distribution based on SRIM (solid line); this distribution is in units of *$(at/cm^3)/(at/cm^2)$*. These units represent the implanted density per unit of the applied dosage

(fluence). For conversion to a physically comparable quantity (ion implanted density vs depth), it should be multiplied with the dosage applied as seen in Figure 2.3.

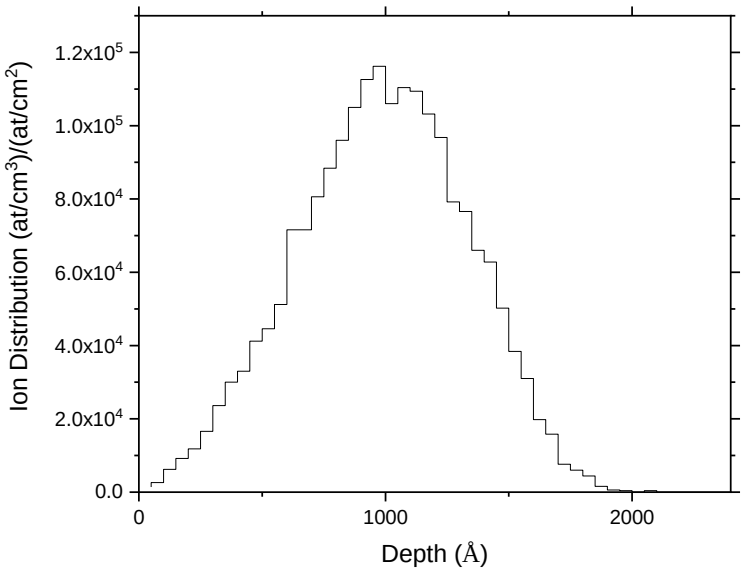

Figure 2.3: Implanted density of Si^- in SiO_2 at 80keV and $2x10^{17}at/cm^2$ fluency calculated via SRIM.

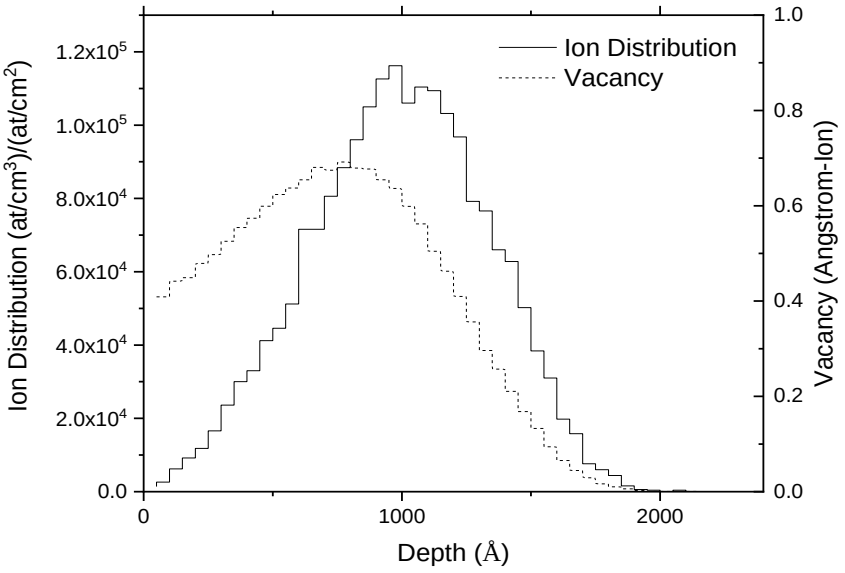

Figure 2.4: SRIM Simulation of Si ions implanted into SiO_2 at 80keV. Depth distribution of Si in SiO_2 substrate along with damage vacancies (for both Si and O) created due to surface ion-solid interactions.

While ions get implanted into the near-surface region, there are also surface sputtering effects that play a significant role at lower (5-50 keV) implantation energies. Figure 2.4 shows the vacancies produced by damage events from ion implantation. SRIM is not able to update the substrate with damage events in real time alongside implantation simulations. While not causing large issues at higher energies due to the sputtering and implantation profiles occurring at different energies, at lower energies surface sputtering tends to overlap alongside the depth profile as seen in Figure 2.4. Due to this effect, the best way to obtain the actual depth profile is to measure an RBS (Section 2.2.1) spectrum that allows for proper characterization of the distribution of the implanted element as a function of depth. It should be noted that since SRIM doesn't provide an instantaneous update of the composition of the substrate with every ion calculation, it cannot take temperature effects and modification of the structure of the material (such as crystallization and recombination) into account and stopping powers (ion energy losses) are not updated based on the change in the crystallinity and composition change.

When an atom is displaced from its original position in its crystalline matrix, it can leave a vacancy and occupy an interstitial site within the substrate lattice. This is known as a Frenkel defect (also known as a Frenkel pair). The first displaced atom is known as the Primary Knock-on Atom (PKA) that can displace other atoms in the substrate lattice, causing a collision cascade. Using Binary Collision Approximation (BCA), computer simulations are able to give us a modified Kinchin-Pease equation (also known as the NRT equation) that gives the number of defects N_d based on an incident energy E_i and displacement energy E_d). If $E_i < E_d$, no displacement occurs. If $E_d < E_i < 2/0.8E_d$, the PKA atom will fill the vacancy left by the displaced target atom and is seen as a replacement collision and is known to cause greater disorder in polyatomic targets than in monoatomic targets. SRIM outputs the number of atomic displacement (vacancies) that are produced by a single ion (Figure 2.4). This can be used to approximate the DPA (Displacement Per Atom) for a known ion dosage via the following equation [8].

$$DPA \cong \frac{\phi \times D(d) \times 10^8}{N} \tag{2.1}$$

Where $D(d)$ is the number of atomic displacement by an ion for a given depth (vacancy/ion/Å) given by SRIM, N (at/cm^3) is the atomic density of the target substrate, ϕ is the dosage (ion/cm^2)

of the incident ion. The factor of 10^8 is to allow for conversion from cm to Å. Typical implantation doses used in this thesis were on the order of 1 x 10^{17} at/cm^2 Si^- in amorphous SiO_2 which results in a peak DPA of approximately 90 displacements per one incident Si atom.

Many defects discussed above can manifest themselves in different forms within a lattice structure, including (in increasing dimensionality) point defects, line defects, planar defects and volume defects [9]. Point defects are 0D defects known to be either caused by solo vacancy sites or interstitial sites. As there is only a single site and no cascading defects, this means that point defects are usually intrinsic to the substrate. Impurities can be a cause of point defects, as they can occupy interstitial locations [10]. Line defects (dislocations) are 1D defects that follow along one dimension in the crystal lattice where there is a change in the lattice structure along a line, usually caused by shear stress on the lattice. Edge dislocations (along the stress) and screw dislocations (perpendicular to stress) are the main two classifications of line defects. Planar defects are 2D defects caused by discontinuities in the crystal lattice across a plane. Usually this occurs as a combination of line defects in a plane. A common type of planar defect is a grain boundary, where one crystal structure ends, and another begins. Usually crystals form independently and grow until they reach each other, forming a planar defect along their interface. Volume defects are also known as voids, where the lattice is deformed around an absence of a large number of atoms. In voids the internal broken bonds form a new surface. Crystalline silicon can become amorphized by a sufficiently large ion dosage. This critical dose depends on the ion, the implantation energy, current and the substrate temperature. For an Si-Si bond strength of 2.31eV and density of 5×10^{22} at/cm^3, a nominal threshold is that damage events for silicon become stable at ~10^{20} to 10^{21} keV/cm^3 and the target will be sufficiently amorphized [9].

Implantation experiments were conducted at the Tandetron accelerator facility at the University of Western Ontario (Figure 2.5) into 1μm and 100nm SiO_2/Si(001) substrates. For the 1μm sample, Si was implanted at 80keV with a dosage of 2×10^{17} ions cm^{-2} at room temperature. For the 100nm sample, two implants were done. A 60keV implant at 5×10^{16} ions cm^{-2} followed by a 40keV implant at 1×10^{17} ions cm^{-2}. After implantation, the implanted samples underwent annealing at 1100ºC with dry N_2 gas to mobilize the atoms enough to nucleate into nanocrystals. A second forming gas annealing (FGA) step at 500ºC, 30 min in forming gas flow (95% N_2, 5%

H_2) was done to allow H_2 to passivate any dangling bonds on the surfaces and interfaces to improve luminescent light emission of these samples.

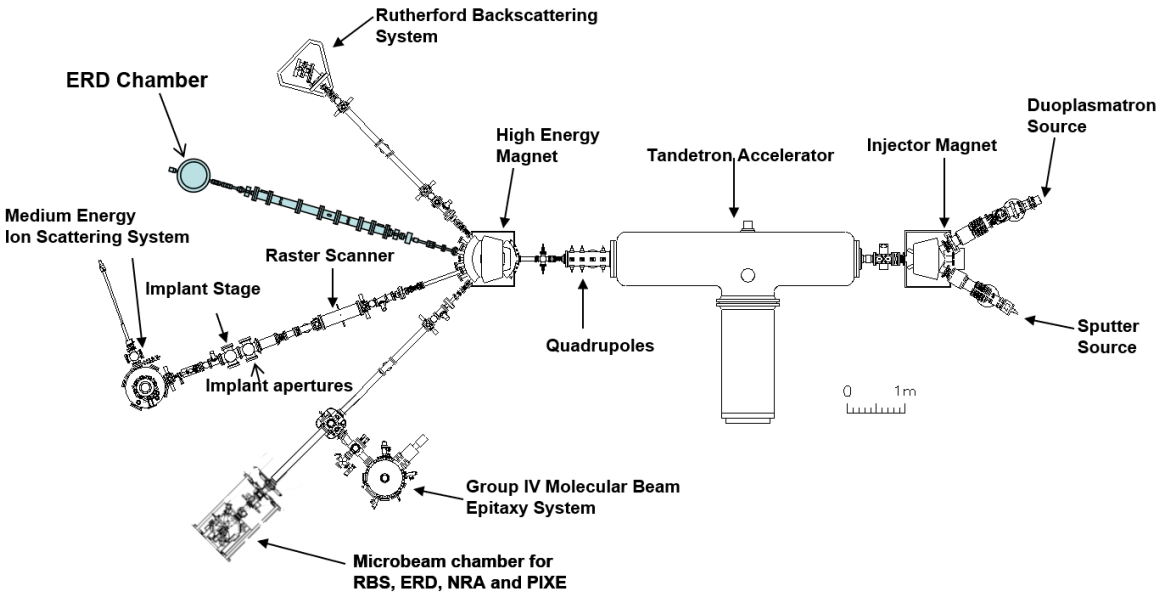

Figure 2.5: Schematic of the Tandetron Accelerator facility at the University of Western Ontario, showing the Rutherford Backscattering (RBS) chamber, elastic recoil detection (ERD) chamber, medium energy ion scattering (MEIS), implant beam line and Microbeam & molecular beam epitaxy (MBE) beamline.

For direct contact electrical measurements, circular Al lateral contact pads were then placed on these samples by e-beam Photolithography at the Nanofabrication facility at the University of Western Ontario with a thickness of 100nm, diameter of 600µm and spacing of 700µm.

2.2. Sample Characterization

In order to study the charge transport mechanisms of Si quantum dots in an SiO_2 matrix, multiple characterization methods were chosen that provide information about the physical structure and electronic properties of the quantum dots and the matrix they are embedded in. This allows better understanding of the sample properties and transport mechanisms. Physical composition characterization includes Rutherford backscattering spectroscopy (RBS) while electronic characterization includes X-ray Photoelectron Spectroscopy, photoluminescence and direct-contact I-V electrical measurements.

2.2.1. Rutherford Backscattering Spectroscopy

RBS involves measuring the energy of the backscattered ions from collisions with atoms on the surface and subsurface layers in the material. The beam line energy and ion can be tuned to probe different depth regions. Most of the RBS analysis in this thesis used a 500 keV He^{2+} beam. Since this measurement involves two nuclei colliding, it can be modelled classically as elastic collisions where the ratio of energy of the incident ion to the backscattered ion is known as the kinematic factor. There is a collision angle dependency for this kinematic factor, where different atomic weights can be differentiated better by scattering angles closer to 170-180º.

$$k = \frac{E_1}{E_2} = \left[\frac{(M_2^2 - M_1^2 \sin^2\theta)^{1/2} + M_1 \cos\theta}{M_1 + M_2}\right]^2 \quad (2.2)$$

Since this method involves ions colliding with a target substrate, there are similar damage and displacement effects that should be thought of. However due to the high energies and low dosages of He^{2+} used in RBS measurements, these effects are not as prominent and do not affect the surface and near surface region of the material. For a 1uC dose of He^{2+}, we can calculate a DPA of 0.0016 displacements/atom, which is much lower than the DPA from implantation calculated earlier.

The advantage of using ion beams is that there is good depth resolution with known cross sections of measured nuclei. Since this process probes the nuclei, the major crystallographic direction of the material can be oriented to the ion beam and it allows for most of the ions to channel through the substrate towards deeper layers (Figure 2.6). This leads to a decrease in counts for the angles with that alignment known as the channeling or aligned geometry.

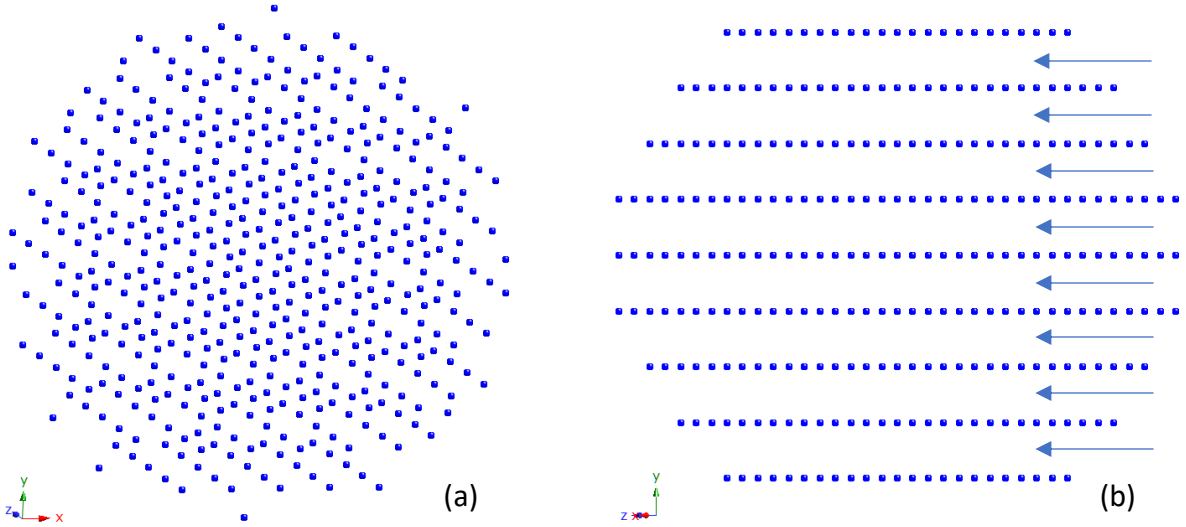

Figure 2.6: Side view on the (a) Si diamond lattice as seen from an arbitrary angle; (b) Same lattice oriented in the [-1.5 0 1] direction by aligning. Which shows where an ion beam would experience channeling effects (arrows shown). Images generated using CrystalMaker®.

When the incident ion beam is carefully aligned to a high-symmetry direction of a crystal, the ions are able to pass through as they are gently steered by the field of the channeling path formed by the rows of atoms. However, thermal vibrations can cause the atom to deviate from this equilibrium potential position, meaning that an ion will eventually collide with such an atom and potentially give off a backscatter ion signal [11]. Another possibility is that the ion collides with an atom that does not follow the high symmetry of the crystal which could be caused by an impurity or defect.

This allows defect and impurity content and depth distribution inside material to be studied using RBS channeling. This method can be extremely powerful in the semiconductor industry where crystal purity is an important factor in manufacturing devices on silicon wafers. RBS can be used to characterize not just impurities in a crystalline sample but also the structural/crystallographic purity of different allotropes/polymorphs of the same materials. For a sample that is continuously bombarded with ions while rotating around an axis of symmetry along an azimuthal direction, the purity of the crystalline structure can be seen based on the periodic changes in total backscattered counts. For a cubic lattice there will be a major drop in counts (a channeling minimum) every 90°, while in a hexagonal lattice the channeling angle repeats every 60°.

Two different software programs SIMNRA [12] and MEISwin [13] were used to analyze the RBS spectra. Before running RBS for our samples, several calibration standards with known atomic densities were measured and fitted to calculate experimental parameters, such as solid angle and the number of incident particles precisely. Most measurements in this thesis used an accurately known implant profile of Sb in Si to precisely calibrate spectra peaks, after which an RBS spectrum can be simulated and matched to the data. The simulated target can be modified with multiple layers, elements, densities and probability of collisions. This modification allows precise simulations of the materials' composition and depth profile.

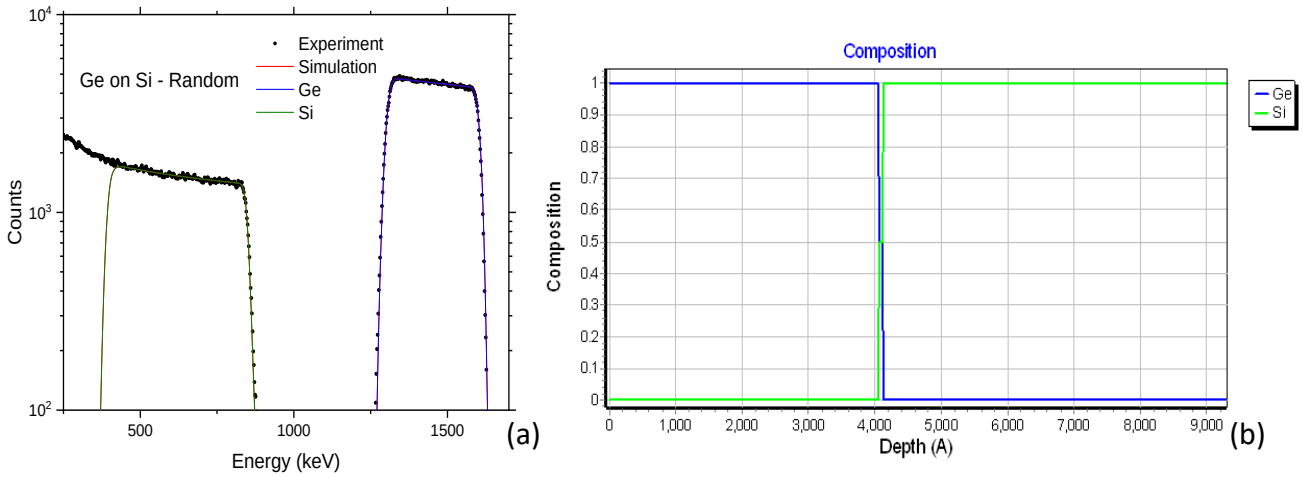

Figure 2.7: (a) RBS experimental data and simulated spectrum of 400nm Ge on Si (100) using 2.5 MeV He^{2+}. (b) Elemental depth profile used to simulate spectrum in (a).

2.2.2. X-ray Photoelectron Spectroscopy

XPS primarily focuses on studying both the chemical state and the elemental composition of a material. Electrons within the material are excited using nearly monochromatic incident photons (for X-rays the incident photon has an energy of 0.1-10keV) and are emitted at different energies (as shown in Figure 2.8 below). The average mean free path for electrons at these energies limit the depth sensitivity of XPS to extremely narrow depths of around 5nm [14]. For a depth profile, the sample must be sputtered and routinely measured at specific depths. The difference in energies are the binding energies of the electrons and is dependent on the orbital that each electron is located in [15]. This results in a full spectrum with multiple peaks corresponding to

different filled orbitals, where binding energy is E_b, kinetic energy is E_k and the incident energy is connected by equation 2.3:

$$E_b = h\nu - E_k \tag{2.3}$$

A typical XPS spectrum is shown in Figure 2.8 showing the number of electrons (counts in detector) vs electron binding energy, E_b. It can be observed that the lower energies probe outer shells that have lower binding energies. While at higher energies, the deeper orbitals that have a higher binding energy are possible to measure. At high enough energies, the Auger peaks begin to dominate the spectrum, making it harder to probe deeper orbitals.

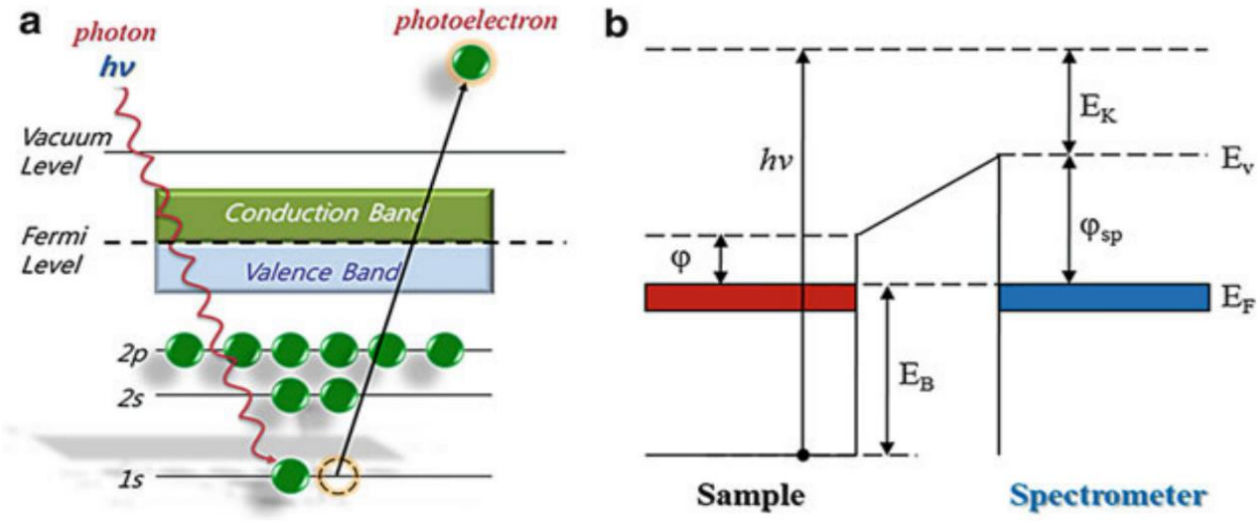

Figure 2.8: (a) Schematic illustration of the core-level photoelectron emission by the photoelectric effect in a metal; (b) Energy-level diagram of the sample and the spectrometer in a core-level photoemission experiment of a metallic sample. [16]

Although it was mentioned earlier that the XPS spectrum probes binding (orbital) energies, it is actually more correct to associate the spectrum to ionization energy. The implication being that bonding will affect the energy of the electron orbital and the spectrum produced. This allows XPS to be used not just for elemental depth analysis but also to give information about how the elements are bonded within the sample [15]. Binding energies can be affected by the electrostatic shielding of other electrons in the atom and removing a valence electron (oxidation) would result in an increase in binding energy, while an addition of a valence electron (reduction) would decrease the binding energy. The scales of these energy shifts are easily measured by the photoelectron energy analyzer (detector).

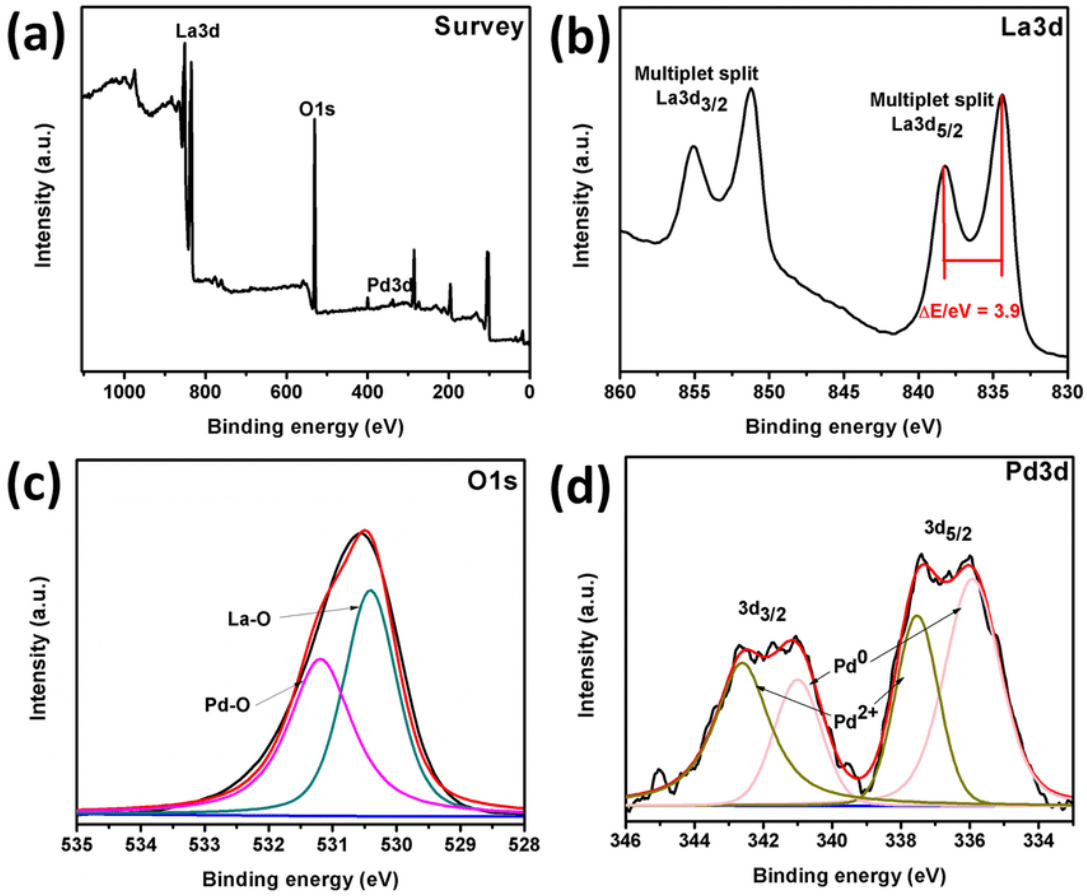

Figure 2.9: (a) Survey XPS spectrum of Pd/La(OH)$_3$ nanocatalyst. High resolution XPS spectra of (b) La 3d orbital, (c) O 1s orbital and (d) Pd 3d orbitals. [17]

2.2.3. Electrical Measurements

Electrical measurements of the sample are taken to better understand the quality and behaviour of samples and to understand what the underlying physical mechanisms of charge transport are for Si QDs embedded in SiO_2. As described in the previous chapter, the samples measured have Al contact pads and create a MOS interface that involves the contact pad, the oxide layer grown on the sample surface and the nanocrystals embedded in the SiO_2.

Two-point contact measurements were made on the sample to conduct multiple measurements and to test for sample homogeneity. Current-voltage (I-V) relationships were measured using a Cleverscope 320A and the DC Keithley Power Supply (Model 230). A custom written LabView program (written by Jack Hendriks) controlled the Keithley output voltage and read the DC current going through the samples. The circuit diagram included in Figure 2.10 shows how the oscilloscope was connected in series in order to measure current values through the sample. The

oscilloscope's internal resistance of 1MΩ was used as the control resistor. To control the probes, Signatone micro positioners were used with probe tips of 25 μm BeCu. Finally, a Faraday cage was introduced to reduce electrical noise and get down to approximately 0.2nA resolution. Benchmarks were made using a 100MΩ resistor in place of the sample (Figure 2.10).

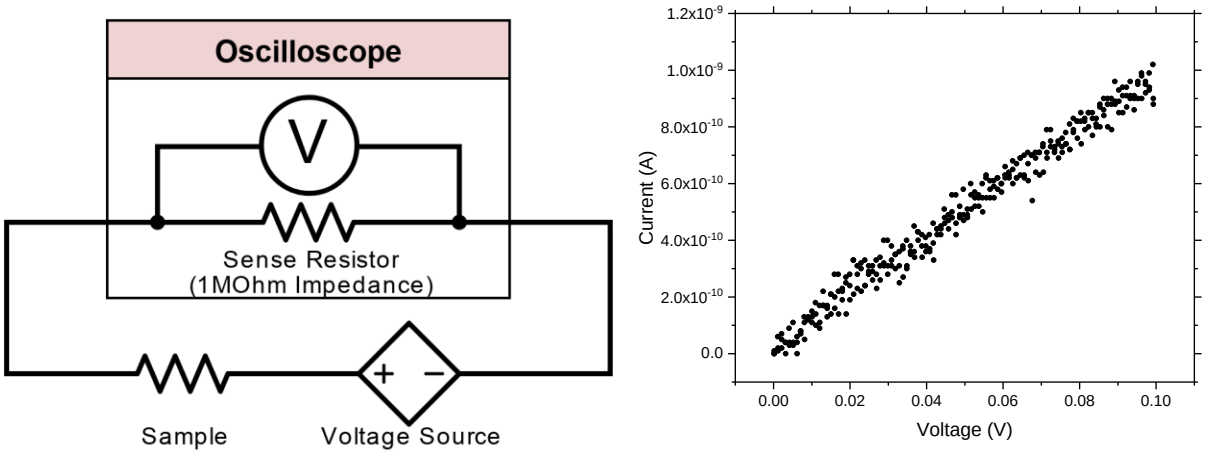

Figure 2.10: (Left) Diagram portraying the experimental setup for measuring currents in a sample. (Right) 100MΩ Resistor baseline showcasing the nA resolution of the experimental setup

2.2.4. Photoluminescence Measurements

In comparison to contact-based electrical measurements, photoluminescence is a contact free technique that probes the electronic structure of the material. It is based around the concept of recombination where the sample is illuminated with a photon of a given energy equal to or greater than the bandgap of the sample. This photon excites an electron in the valence band to an excited state creating an exciton, after which it relaxes and recombines with the hole in a process known as recombination (See Chapter 1). As seen earlier, this recombination process can be radiative with the emission of a photon, or non-radiative with coupling to phonons.

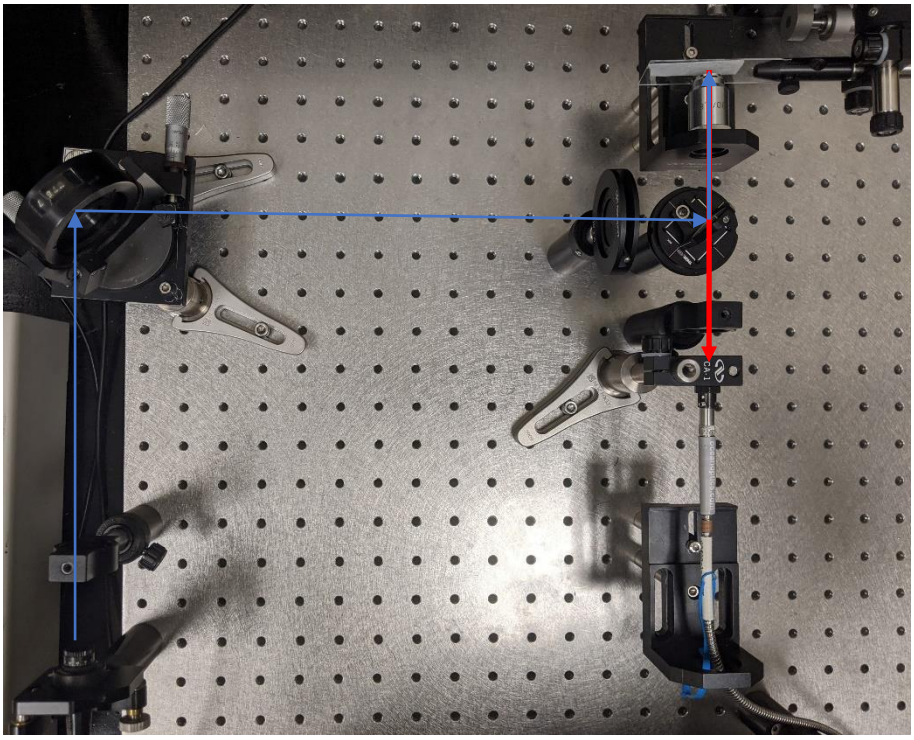

Figure 2.11: PL setup showcasing the 405nm beam path (blue) and the PL emission path (red)

Photoluminescence aims to study the radiative recombination process of the sample by measuring the light emitted by the sample during the recombination process. The PL apparatus is set up on an optical bench with a light source at frequencies close to the band gap of the sample. The bench setup is designed in such a way that the reflected incident beam and the PL emission of the sample are in different directions. In many cases, a high pass filter is used to prevent scattered incident rays from entering the spectrometer while not impeding the emission wavelengths. Inside the spectrometer is a diffraction grating that directs the different wavelengths into an array of photodetectors, that is then logged into a computer to create a spectrum of the sample. A background measurement is usually taken preceding the sample measurement. This is done to ensure that background noise can be removed from the data. In the setup the light source is a Class 3B laser diode at 406nm with an output power of 10.6mW, the laser light was filtered through a bandpass filter centered at 405nm and the emission beam was filtered with a high pass filter >450nm. The spectrometer used was a FLAME-S-XR1-ES spectrometer with a diffraction grating of 500g/mm and 25µm slit, which has a corresponding wavelength range of 200-1050nm and resolution of 1.9nm.

2.3. References

[1] M. Henini, Molecular Beam Epitaxy: From Research to Mass Production, Newnes, 2012.

[2] W.P. McCray, MBE deserves a place in the history books, Nature Nanotechnology, 2 (2007) 259-261.

[3] B. Mayer, A. Regler, S. Sterzl, T. Stettner, G. Koblmüller, M. Kaniber, B. Lingnau, K. Lüdge, J.J. Finley, Long-term mutual phase locking of picosecond pulse pairs generated by a semiconductor nanowire laser, Nature Communications, 8 (2017) 15521.

[4] A. Abdelal, Silicon Nanostructures Deposited by Molecular Beam Epitaxy on Silicon Oxide, Physics & Astronomy University of Western Ontario, 2017.

[5] A.P. Alivisatos, Semiconductor Clusters, Nanocrystals, and Quantum Dots, Science, 271 (1996) 933-937.

[6] C.A. Straede, N.J. Mikkelsen, Implementation of ion implantation in European industry, Surface and Coatings Technology, 84 (1996) 567-573.

[7] J.F. Ziegler, M.D. Ziegler, J.P. Biersack, SRIM - The stopping and range of ions in matter (2010), ADS, DOI (2010).

[8] M. Li, M.A. Kirk, P.M. Baldo, D. Xu, B.D. Wirth, Study of defect evolution by TEM with in situ ion irradiation and coordinated modeling, Philosophical Magazine, 92 (2012) 2048-2078.

[9] J.F. Gibbons, Ion implantation in semiconductors—Part II: Damage production and annealing, Proceedings of the IEEE, 60 (1972) 1062-1096.

[10] L.S. Gianfranco Pacchioni, David L. Griscom, Defects in SiO2 and Related Dielectrics: Science and Technology, Springer Science, 2000.

[11] L.C. Feldman, J.W. Mayer, S.T.A. Picraux, Materials analysis by ion channeling: submicron crystallography, Academic Press, 2012.

[12] M. Mayer, SIMNRA user's guide, Max-Planck-Institut für Plasmaphysik Garching, 1997.

[13] T. Nishimura, Computer simulation program for medium-energy ion scattering and Rutherford backscattering spectrometry, Nuclear Instruments and Methods in Physics Research Section B: Beam Interactions with Materials and Atoms, 371 (2016) 97-100.

[14] V.P. W. H. Doh, S. Zafeiratos, Applications of Synchrotron-Based X-Ray Photoelectron Spectroscopy in the Characterization of Nanomaterials, Springer-Verlag Berlin Heidelber, 2015, pp. 317-366.

[15] C.S. Fadley, X-ray photoelectron spectroscopy: Progress and perspectives, Journal of Electron Spectroscopy and Related Phenomena, 178-179 (2010) 2-32.

[16] W.H. Doh, V. Papaefthimiou, S. Zafeiratos, Applications of Synchrotron-Based X-Ray Photoelectron Spectroscopy in the Characterization of Nanomaterials, Springer-Verlag Berlin Heidelber, 2015, pp. 317-366.

[17] A.B. Yousaf, M. Imran, M. Farooq, P. Kasak, Interfacial Phenomenon and Nanostructural Enhancements in Palladium Loaded Lanthanum Hydroxide Nanorods for Heterogeneous Catalytic Applications, Scientific Reports, 8 (2018) 4354.

Chapter 3

3. Electrical Transport in Si Quantum Structures

3.1. Motivation

Nanomaterials such as semiconducting quantum dots (QD) are of immense interest and value in optoelectronics and nanotechnology. One can control the bandgap by the QD size, and the majority of studies in the literature have focused on optical properties, notably their photoluminescence (PL). However, there have been fewer publications on the electrical properties and charge transport mechanisms and their connection to their optical response. Models for electron transport in ligand-capped ensembles of QD's (typically II-IV compound semiconductors) have been proposed [1]. We expect to see a change in transport mechanisms of QDs as the density changes, especially around a percolation threshold where transport via QDs transport can be ascribed to a QW structure. Currently QDs in colloidal solutions have been extensively studied, with their optical responses being well understood and applied in consumer products such as QD-LED televisions. However, those systems are incompatible with solid state systems with fabrication processes in the semiconductor industry: those may be controlled by different models.

This study aims to gain better fundamental understanding of charge transport properties Si QD's and quantum wells in SiO_2 at room temperature. We focus on solid state forms of Si quantum systems in SiO_2 as the goal is compatibility with the current semiconductor industry fabrication processes. Molecular beam epitaxy (MBE) and ion implantation fabrication processes were selected for Si quantum structure fabrication. We would like to better understand the connection between the properties of individual QDs and the connectivity of the system (e.g., in the vicinity of percolation threshold). Based on models introduced in Section 1.2, we formulate a band energy model for our sample in Figure 3.1, where Δs is the thickness of the effective oxide thickness, a is the mean distance between QDs, D is the diameter of an individual Si-QD and Φ_1 & Φ_2 are the work functions of each contact point. We can define a percolation threshold for when $D>>a$, where the Si QDs can be thought of as a QW structure. Additionally, there are defect trap sites in the SiO_2 matrix itself (denoted by red lines in Figure 3.1)

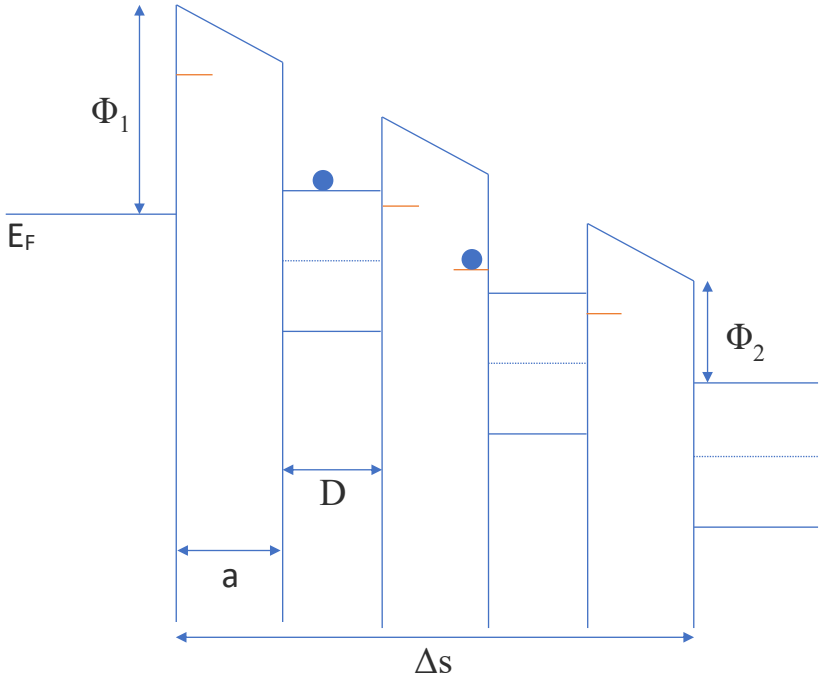

Figure 3.1: Band diagram model of solid-state Si QDs in SiO_2 in an E-Field, where red lines denote defects in SiO_2, and blue dots are charges moving through the sample

3.2. Experimental Details

Sample Preparation

Si quantum structures were fabricated via two solid-state fabrication processes: MBE and ion implantation, using SiO_2 dielectric layers. Si quantum wells were made by Aysegul Abdelal [2] using a UHV MBE chamber (Kurt Lesker), containing a source of Si (Alfa Aesar, 99.9999% purity), that was evaporated from a water-cooled graphite crucible using electron-beam heating. The deposition rate was controlled using a quartz crystal monitor (with typical value of less than 0.2Å/s) and was calibrated by independent Rutherford backscattering measurements with a deposition on a carbon substrate [3]. The substrates were heated by an e-beam heater (VG Ltd., Hastings), and their temperature was probed by two thermocouples (OMEGA). We used 0.5mm thick Cz n-doped Si(001) wafers (0.001-0.005 Ω/cm) with lateral dimensions of 10×8 mm, as our substrates. Deposition temperatures in the 25-800°C range have been tested, however all samples presented here were deposited at 300°C. A 20nm SiO_2 layer was deposited by plasma-enhanced chemical vapor deposition (PECVD) on top of the Si QW sample, after which 100nm

thick Al contact pads were deposited on top of the SiO_2 layer using e-beam/photolithography at the Western Nanofabrication facility. In order to produce statistically robust current-voltage characteristics, a 5×5 array of Al triangular contact pads was produced with lateral dimensions (height) of 710±5 nm and 700μm spacing between individual pads.

Ion implantation was performed at the Western Tandetron accelerator facility. Si^- ions were implanted into two different substrates: (1) a 1μm SiO_2/n-Si(001) sample at 80keV with a dose of 2×10^{17} atoms/cm^2, and (2) a 100nm SiO_2/n-Si(001) (3-10 Ohm cm) at 60keV, 5×10^{16}atoms/cm^2 and 40keV, 1×10^{17}atoms/cm^2 consecutively. Both samples were annealed at 1100^0C (60 minutes, dry N_2) followed by a 500^{o}C anneal, 30 minutes in forming gas (95% N_2, 5% H_2). This second annealing step is done to passivate dangling bonds at the Si-SiO_2 interfaces. For contact measurements, 100nm thick Al contact pads were placed using e-beam lithography with a diameter of 600μm and a 700μm spacing in between. Ion implantation experiments were simulated using Stopping and Range of Ions in Matter (SRIM) to model and predict the implantation depth and density. These models were later verified via Rutherford Backscattering Spectroscopy (RBS).

Characterization

Rutherford Backscattering Spectroscopy (RBS) was performed to monitor the Si depth distribution in the implanted samples, as well as diffusion during the annealing process. RBS measurements were done using a rotating random geometry with a detector mounted at 170^{o}C, using a $^4He^+$ beam at 0.5 MeV or 2.0 MeV. A Sb-implanted amorphous silicon sample with a known total Sb content of 4.71×10^{15} atoms/cm^2 was utilized to measure the detector solid angle and accurately determine Si depth profiles. Backscattered ion energy distributions were simulated using SIMNRA and MEISwin software [4, 5]. The simulated target can be modified with multiple layers, elements, densities and probability of collisions. These modifications allow for precise simulation of material composition and depth profiles, allowing us to closely match the RBS data and quantify stoichiometry of SiO_x films, and their depth distribution.

X-Ray photoelectron spectroscopy (XPS) was analyzed to monitor the oxidation states of Si in the sample. The setup used a Kratox AXIS Supra spectrometer using a monochromatic Al K(alpha) source (15mA, 15kV). The instrument work function was calibrated to give a binding

energy of 83.96 eV for the Au 4f7/2 line for metallic gold and the spectrometer dispersion was adjusted to give a binding energy of 932.62 eV for the Cu 2p3/2 line of metallic copper. The Kratos charge neutralizer system was used on all samples. Survey scan analyses were carried out with an area of 300 × 700 microns and a pass energy of 160 eV. High resolution analyses were carried out of 300 × 700 microns as well, with a pass energy of 20 eV. Spectra have been charge-corrected as needed to the main line of the carbon 1s spectrum (adventitious carbon) set to 284.8 eV. Spectra were analyzed using the CasaXPS software.

Photoluminescence spectroscopy (PL) was performed to probe the electronic properties of the sample with a Class 3B laser diode at 406nm with an output power of 10.6mW. The laser light was filtered through a bandpass filter centered at 405nm and the emission beam was filtered with a high pass filter >450nm. The spectrometer used was a FLAME-S-XR1-ES spectrometer with a diffraction grating of 500g/mm and 25μm slit, which has a corresponding wavelength range of 200-1050nm and resolution of 1.9nm. Both studies were used to better understand the interface layer between the Si QD's and SiO_2 substrate

Finally, 2-probe electrical measurements were performed on the sample to better understand charge transport in ensembles of QD's with VI curves being generated and then modeled. E-beam lithography was used to place 100nm thick Al contact pads with 1.3mm spacing (Western Nanofab). Current-voltage (I-V) relationships were measured using a Keithley DC power supply (Model 230) and a Cleverscope 320A digital oscilloscope. A custom LabView program (written by Jack Hendriks of the University of Western Ontario) was used to simultaneously control the Keithley output voltage and read the DC current through the samples. Signatone micro-positioners were used with 25 μm BeCu probe tips. This allowed us to get the system to around 0.2nA resolution. Benchmarks were made using a 100MΩ resistor in the place of a sample. MBE samples had pre-placed lateral Al probes to use. At the Tandetron facility, the minimum implant energy of negatively charged Si ions is around 30keV. This leads to a depth profile that is approximately 100nm wide. Hence a 100nm thick oxide sample was used for implantation and was then probed longitudinally.

3.3. Results and Discussion

3.3.1. Depth Profiling during implantation process

Quantification of the Si content of the SiO_2 top layer in the MBE samples is challenging since an ultra-thin layer of Si quantum well (QW) is sandwiched between 1μm SiO_2 with thermally grown SiO_2 on top. Hence the MBE deposition process was repeated on a diamond like carbon (DLC) substrate to verify the thickness of the Si QW layer. Ultra-thin Si layers convert to SiO_2 at ambient conditions, and thickness analysis of these SiO_2 layers was done by RBS. A representative RBS spectrum for one of Si QW samples is shown in Figure 3.2. The results verify that thickness of the SiO_2 layer is 4.5 ± 0.5 nm, and this corresponds to an original Si QW thickness of 2.2 ± 0.5 nm.

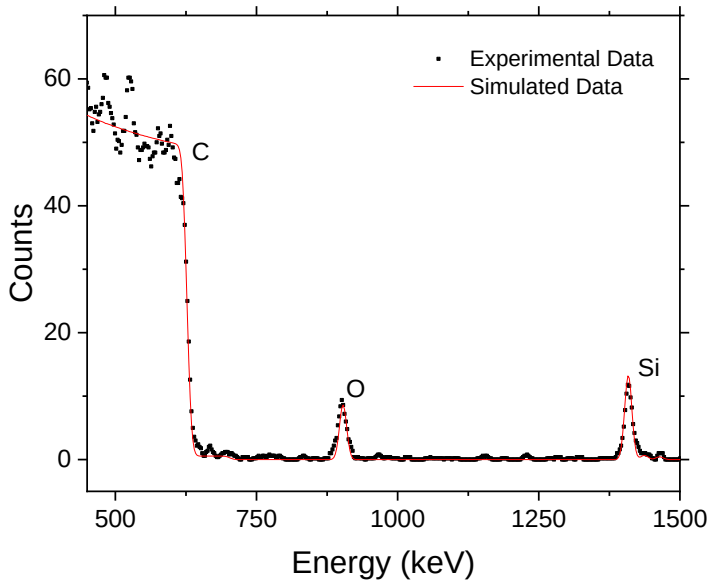

Figure 3.2: 2.0 MeV RBS spectrum of MBE grown Si-QDs on carbon substrate with native SiO_2 on top.

The location and distribution of implanted Si after implantation and following high-temperature annealing to precipitate Si QDs in SiO_2 was determined from Rutherford backscattering measurements shown in Figure 3.3(a). RBS spectra in Figure 3.3 show the Si surface and near-surface distribution, with the full energy spectra shown in Appendix B. It confirms the presence of excess silicon in the oxide layer, compared to the SiO_2 thin film before implantation. RBS

measurements were taken both before and after annealing to monitor the diffusion of Si in SiO_2, during the growth of Si QDs at high temperature. From the shift of Si distrubution for as-implanted sample (blue curve) to a lower energy for Si QDs/SiO_2 (red curve) we conclude that the process of Si QDs growth is accompanied by some small diffusion and redistribution of Si as a function of depth. In order to quantify these results, simulations of RBS spectra were done using both SIMNRA and MEISwin software.

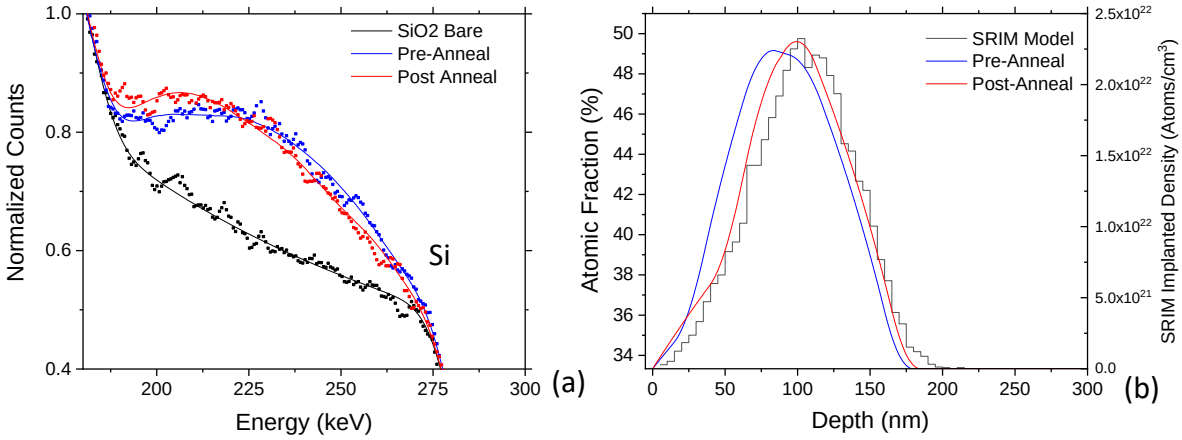

Figure 3.3: (a) Rutherford backscattering spectra (0.5 MeV He^+) for pure 1μm SiO_2 /Si(001) overlaid with implanted Si in SiO_2 both pre and post anneal. (b) Implanted Si depth profile deduced from RBS spectra compared to SRIM model for implantation

Figure 3.3(b) details the difference between the SRIM simulation (black curve) and the Si profile deduced from RBS results for the as-implanted sample, and for the annealed sample with Si QDs. The small linear shift is expected between the SRIM simulation and depth profiles due to the effects of sputtering at low implantation energies. Moreover, we note that during the annealing process necessary for Si QDs growth, the Si atoms are mobile enough to move deeper (by approximately 70 nm) into the SiO_2 sample and stabilize at a depth distribution that closely matches the SRIM data. Additionally, from the integration of the Si peak yield, we verify the Si implanted dose in the sample to be $(1.92 \pm 0.09)\times 10^{17}$ at/cm^2 is within 5% accuracy of the intended dose of $(2.0 \pm 0.1)\times 10^{17}$ at/cm^2.

Si QDs distributions were analyzed in detail using high-resolution transmission electron microscopy (HRTEM) in the past (Figure 3.4) [6]. Note that identical Si QDs preparation procedures have been used in this project and for samples characterized by Mokry, et al. The

mean Si QD size was found to be in the 1.67-1.86 nm range, with Si QDs increasing in size with increasing depth below the surface until a depth of 180 nm, after which size decreases. Further examination of HRTEM images presented there indicate that individual Si QDs are separated by SiO_2 with an average thickness of 2.0±0.6 nm.

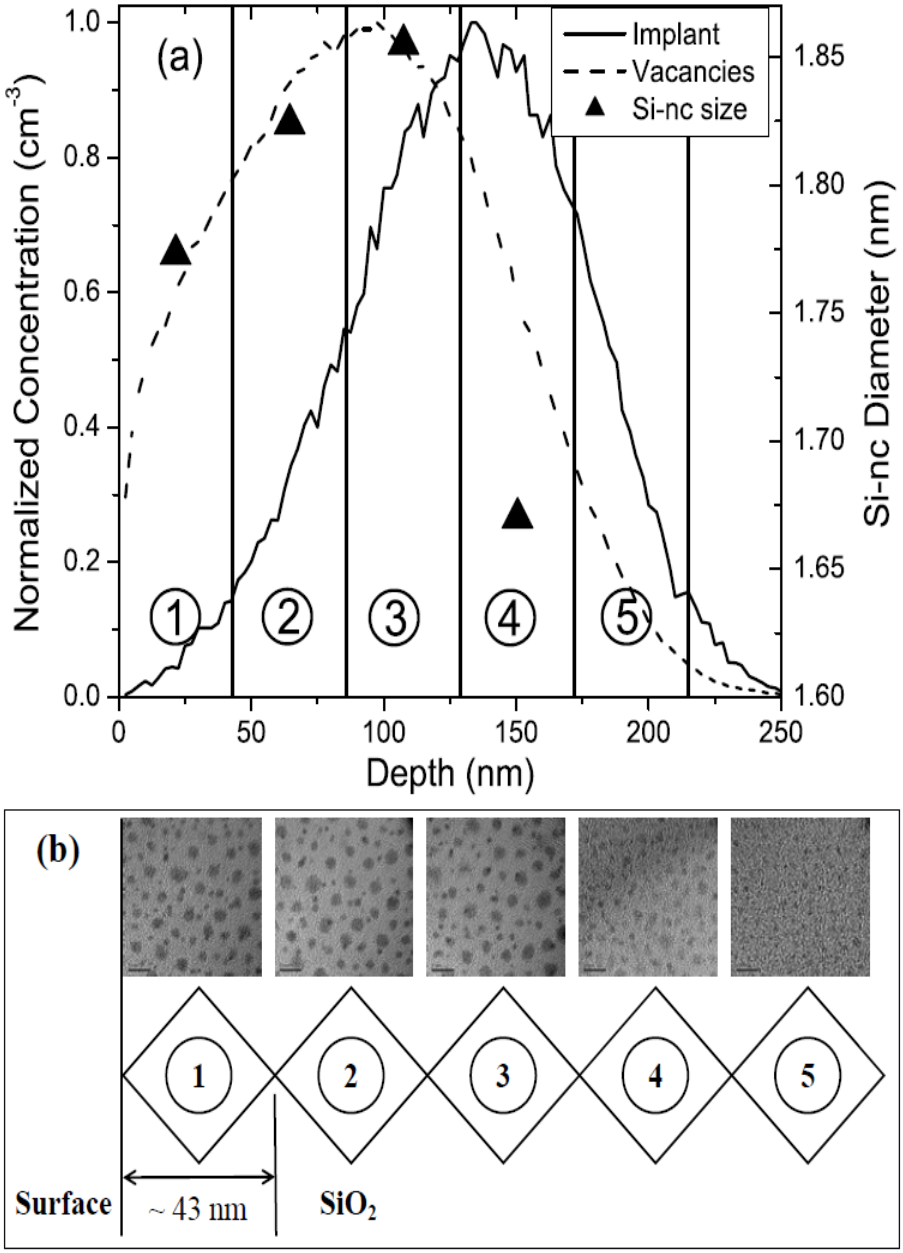

Figure 3.4: (a) SRIM simulation of the implantation profile and vacancy-type defect distribution at 90 keV plotted with the mean size of the Si-nc determined by TEM. (b) TEM images including an outline showing their location and orientation relative to the oxide film and the surface. Adopted from [6]

3.3.2. Understanding the Si QD-SiO_2 interface

XPS analysis of Si QDs/SiO_2 interface

Previous XPS measurements taken on Si implanted into SiO_2 were used. The XPS spectra was calibrated around an Si sample peak and SiO_2 peak. Due to the non-conductive nature of the sample, charging effects on samples with an SiO_2 substrate broaden the Si $2p_{1/2}$ and Si $2p_{3/2}$ peaks and make it hard to resolve orbital spin coupling effects.

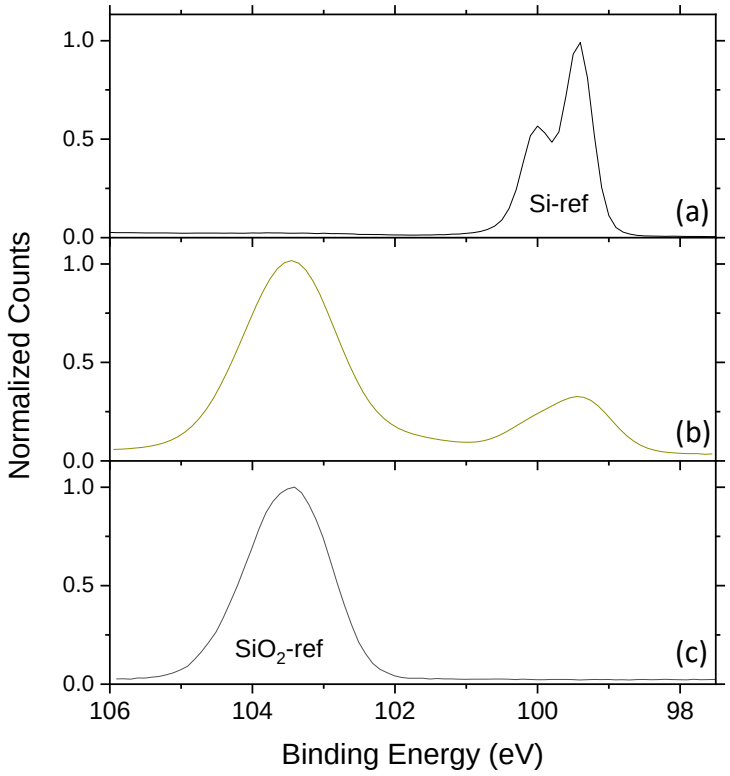

Figure 3.5: XPS Spectra for (b) Si 2p peaks for Si QDs in SiO_2, compared to (a) Si-ref and (c) SiO_2-ref.

Results show that there is a sizeable portion of Si-Si bonding in the sample, of which some fraction of those may correspond to Si-QDs. However undercoordinated Si atoms can be observed as Si(II)+Si(III) states in the sample, those can be ascribed to the interface layer between Si QDs and SiO_2 matrix, or other Si interstitials in SiO_2, that did not precipitate fully into QDs after implantation and anneal. Detailed fitting of XPS results is presented in Figure 3.6 below. While those two states (Si(II) and Si(III)) are unresolvable from each other, they can be

distinguished from the Si and Si(IV) states. For the fittings, a spin orbit separation of 0.64eV was used for all peaks (Si (0), Si (III), and Si(IV)). The Si(IV) state corresponds to SiO_2 bonding and accounts for 73.6% of the sample wt. while the Si(0) state corresponds to the interior bonded atoms of an Si QD and account for 18.8% of the sample wt. while interface bonded atoms correspond to 7.6% wt. Using these measurements, the ratio of implanted Si(0) %wt. to Si(IV) %wt. measured by XPS is compared to the total implanted silicon dose (from RBS measurements) to estimate the amount of Si atoms that condensed into Si QDs during the annealing process, calculated to be around 47%.

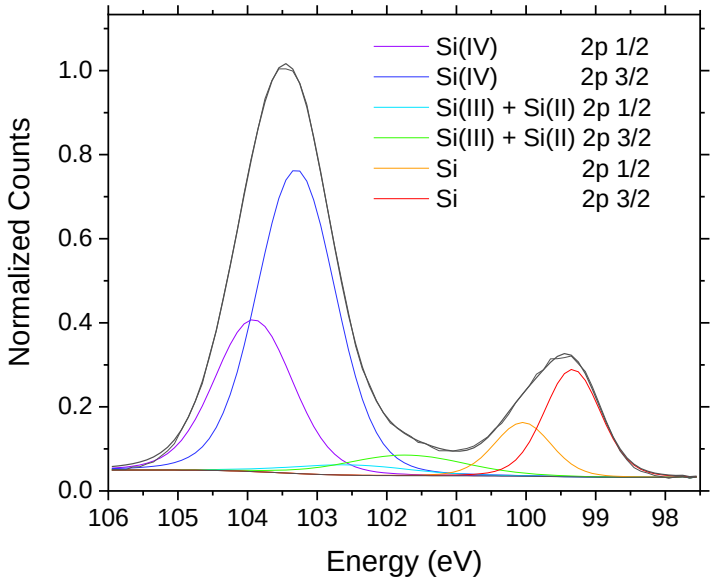

Figure 3.6: XPS spectra deconvolution showing Si (IV) states, Si (II, III) states and Si 0 states peak positions.

Photoluminescence

While the MBE samples did not show any measurable photoluminescence (PL), the ion implanted sample exhibit a strong multi peak PL spectrum with maximum at 1.62eV (~ 764 nm) as seen in Figure 3.7(a). An average Si QD diameter of 1.69nm is calculated using the maximum of PL spectrum and Equation 1.2 (with $E_g(\infty) = 1.1$eV and $A = 1.39$ eV/nm^2). This value matches well with QD size distributions the 1.67-1.86 nm range, as determined by HRTEM images by Mokry et al. The confinement constant is taken from the 3D medium confinement model proposed by E. Barbagiovanni [7]. Additionally, the emission energies were matched to another

model produced by Ledoux [8] (Figure 3.7(b)). The 3D Strong model, while shown in Figure 3.7(b), is less likely as it typically leads to diameters greater than 2.5nm, which is larger than the exciton radius of a hole.

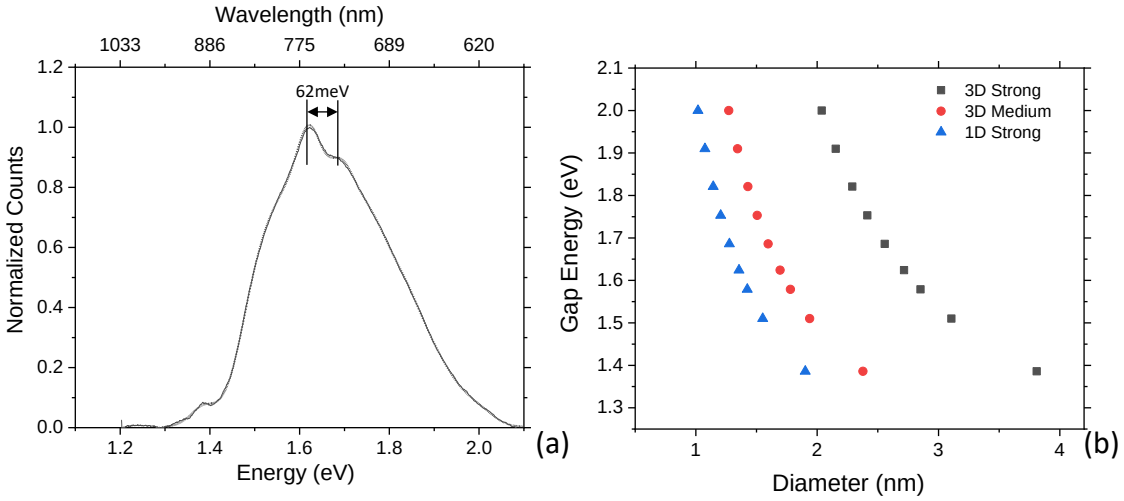

Figure 3.7: (a) PL spectrum of Si QDs in SiO_2 formed via SI implantation, (b) Different confinement models relating measured spectra peaks to QD size.

In addition to a visible peak separation, the PL emission is non-symmetrical. This can be attributed to a non-gaussian distribution of quantum dot size. The peak separation is measured to be $\Delta E = 0.062 \pm 0.006$ eV. This difference in energy is comparable to the splitting of PL spectra in the Configurational-Coordinate (CC) model at the long wavelength optical phonon frequency $\hbar\omega_o$=64.38meV [9] where the energy is split into multiple bands due to the vibrational energy states [10]. Further deconvolution of the spectra fit following the CC model allows for a much more precise fit to the asymmetry, however this resulted in fitting the spectra with a minimum of 4 peaks or more, leading to a case of overparameterization in the model. (Figure 3.8)

Other possible causes of these peaks could be defect band levels. Previous studies have shown the importance of understanding the Si/SiO_2 interface and have modelled the influence of the interface oxidation degree on bandgap and associated electronic properties of the QD/substrate system [11]. Currently, the role of interface defects is not fully understood with many studies suggesting their importance [12] or insignificance [13] in radiative recombination. However as shown in Figure 1.4, a change in oxidation state would account for band gap shift on the order of

400meV or more and does not match up to the gap measured. To further probe the Si/SiO_2 interface, a spectrometer going further towards the IR wavelengths is required.

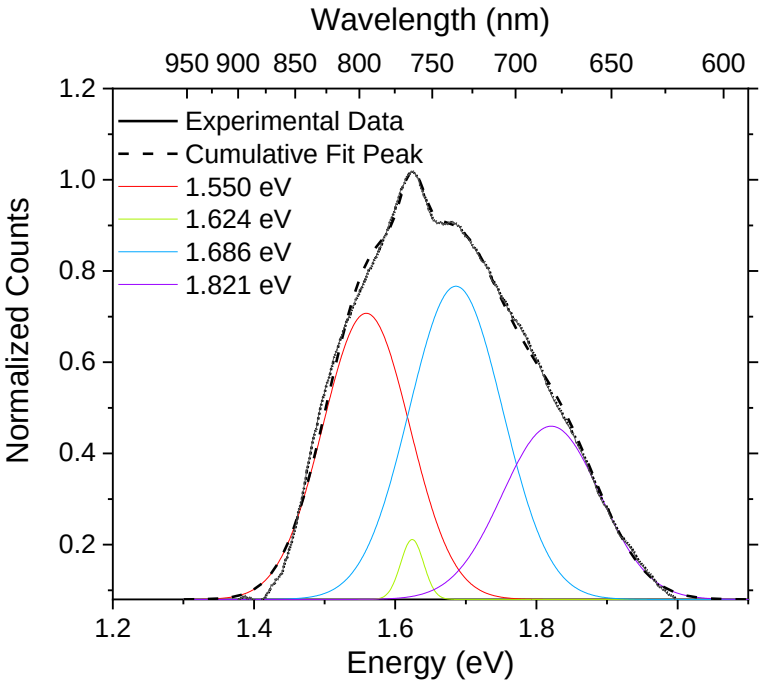

Figure 3.8: PL spectrum deconvoluted to four constituent peaks with a separation of a multiple of 64meV.

3.3.3. Electrical Characterization

Multiple room temperature measurements were taken on the same sample via different contact pads. While there was a substantial variance in measurements between different contact pads, 3 pad-pair combinations were able to give reasonably consistent results and are used as the basis of the following measurements. With the oxide layer being 10nm thick, lateral I-V measurements will have an effective oxide thickness of 20nm that was used in the models [2]. A maximum limit on the current densities were calculated based on the area of the 100nm thick triangular contact pad of 710µm height (2.91×10^{-3} cm^2) however the current path should be smaller than that since the current path is lateral between two contact pads on the same side of the device. To ensure that this is not an issue, any physical parameters that were extracted from the model are not dependent on the scaling of the current density. Similarly, the oxide layer in the ion implanted sample was 100nm thick and had a 100nm thick Al circular contact pad of diameter of 600µm

(2.83×10^{-3} cm^2) and 700μm lateral spacing. For the ion implanted sample, measurements were taken between the Al contact pad and the Si substrate of the sample.

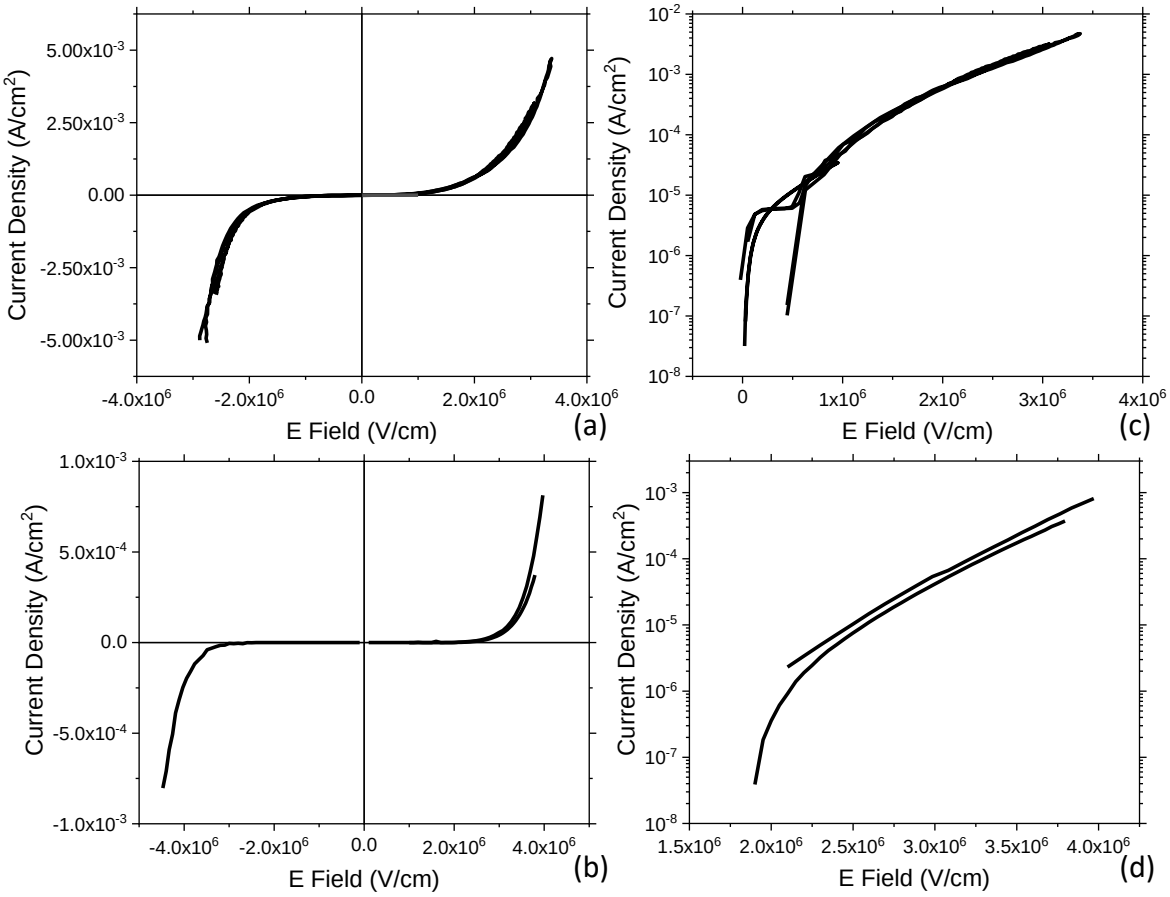

Figure 3.9: Current-voltage characteristics of (a) Si QWs fabricated by molecular beam epitaxy with SiO_2 matrix and Al contacts (b) Si QDs fabricated by ion implantation. Different curves correspond to different pairs of Al contact pads. (c, d) Results plotted logarithmically for the positive values of current and voltage for both samples, respectively.

Fowler Nordheim Tunneling

Fowler Nordheim involves the tunneling of an electron through a potential barrier in a high enough electric field. As expected, Fowler-Nordheim tunneling does not take effect until a high enough threshold E_{FN}, measured by some to be around 1MV/cm [14-16]. A standard Fowler-Nordheim relationship is as follows

$$J = \left(\frac{q^3E^2}{8\pi hq\Phi_b}\right) exp\left[\frac{-8(2qm_T^*)}{3hE}\Phi_b^{3/2}\right] \quad (3.1)$$

Which as we see in Figure 3.10 gives us a straight line for *log* (J/E^2) α $(1/E)$ plot beyond 1MV/cm. For a given FN-representation plot, the barrier height of the tunneling mechanism can be obtained from the slope via the following equation:

$$slope = -6.83x10^7 \sqrt{\left(\frac{m_T^*}{m_0}\right)\Phi_b^3}\left(\frac{cm}{V}\right) \quad (3.2)$$

where m_t^* is the effective mass of the majority carrier and Φ_b is the barrier height of the semiconductor-oxide interface. Assuming an effective electron mass of $0.33m_0$ in SiO_2, a barrier height of approximately 0.28 ± 0.10 eV is obtained. This value is lower than previously measured off stoichiometric silicon dioxide film measurements of 0.6eV to 0.7eV [14, 16] but can be attributed to a higher density of Si quantum structures in the matrix, further lowering the barrier height due to field enhancement effects.

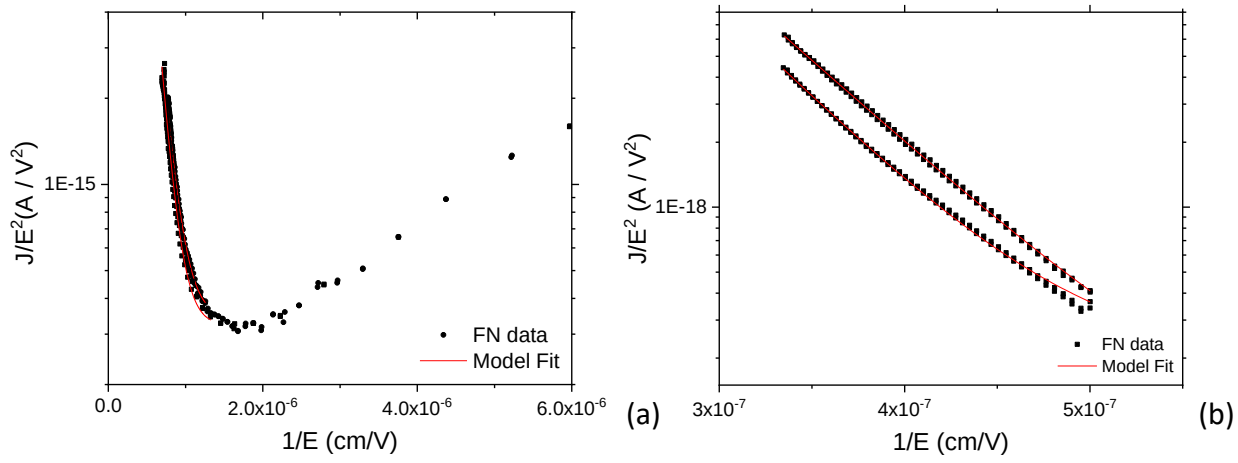

Figure 3.10: Fowler Nordheim representation of (a) MBE grown Si-QWs in SiO_2 (b) Ion implanted Si-QDs in SiO_2 for multiple Al pads

The ion implanted sample shows an onset of FN tunneling at around 5 MV/cm, before which there is no appreciable current measured. Assuming the same electron effective mass of $0.33m_0$

in SiO_2, we can extract the barrier height to be 0.69 ± 0.13 eV, which agrees with previous studies of stoichiometric silicon dioxide film measurements of 0.6eV to 0.7eV [14, 16]. (Table 3.1)

Poole-Frenkel Model

Being a modification of Schottky emission, we expect to see Poole Frenkel emissions at high electric fields, and we see its onset at a similar value as E_{FN} threshold of around 1MV/cm in the QW sample. This is similarly reported in Pi et al [14] and confirms room temperature measured onsets of both Fowler-Nordheim and Poole-Frenkel mechanisms. Past research shows that, while PF involves free electrons emitted from donor centers (N_d) [17], an increase in defect sites such as trapping and acceptor centers (N_t) will lead to an increase in free electrons from donor centers. This dependence on both N_d and N_t can change how PF emissions are modeled. For N_d=N_t we follow the modified/anomalous Poole Frenkel effect [17] where the slope of the graph is halved, equaling the slope of the Schottky plot. The current density for this modified Poole-Frenkel model is given to be

$$J = q\mu N_c E \ exp\left[\frac{-q\left(\Phi_T - \sqrt{qE/4\pi\epsilon_r\epsilon_0}\right)}{2kT}\right] \tag{3.3}$$

Since Poole Frenkel is a trap-bulk assisted mechanism, its observation gives credence to the idea that the quantum dots or Si-SiO_2 interface themselves are trap sites that allow for the Poole-Frenkel mechanism. In measuring the slope of a PF plot, the dielectric value of the MBE grown QW system is measured to be in the range of $3.66 < \varepsilon_r/\varepsilon_0 < 11.73$. Following through with $n \propto \varepsilon^{1/2}$, we get a refractive index of around $1.96 < n < 3.45$. This large discrepancy is attributed to the non-symmetry of the voltage current curve between the forward and reverse bias. The high values of refractive index are characteristic of non-stoichiometric silicon oxide films with high silicon content [18, 19]. For reference bulk SiO_2 has a refractive index of 1.54. The ion implanted QDs sample had a more consistent PF slope that corresponded to a refractive index of 1.73 ± 0.15, which also is attributed to a higher silicon content in an oxide layer (Table 3.1)

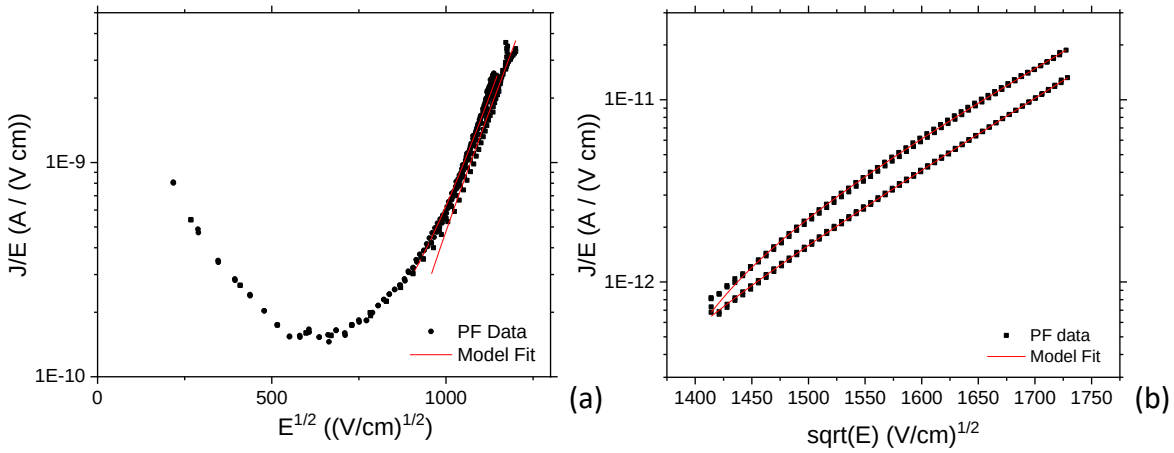

Figure 3.11: Poole Frenkel representation of (a) MBE-grown Si QWs in SiO_2. (b) Ion implanted Si-QDs in SiO_2, both showing PF emission for multiple Al pads

Hopping trap sites model

Alongside Poole-Frenkel, the hopping conduction model involves tunneling between trap sites. While PF emissions involve thermionic jumping between trap sites, hopping conduction involves direct tunneling of charge from one trap site to another. Since the carrier energy is lower than the barrier, we should still expect to see this model at lower electric fields. The expression for hopping conduction is

$$J = qan_e\nu \, exp\left[\frac{qa_tE}{kT} - \frac{E_a}{kT}\right] \tag{3.4}$$

where E_a is the activation energy, a_t is the mean spacing between trap sites, n_e is the electron concentration in the dielectric conduction band and ν is the frequency of thermal vibrations at the trap sites. Plotting ln(J) vs E and measuring the slope allows us to measure the mean spacing between trap sites. Trap spacing is measured to be under a nanometer, which is incredibly small, even for spacing between quantum dots. However, at high enough densities, a percolation threshold may be achieved where quantum dots are nearly touching. At this point the hopping mechanism is on the order of the Si-SiO_2 interface width.

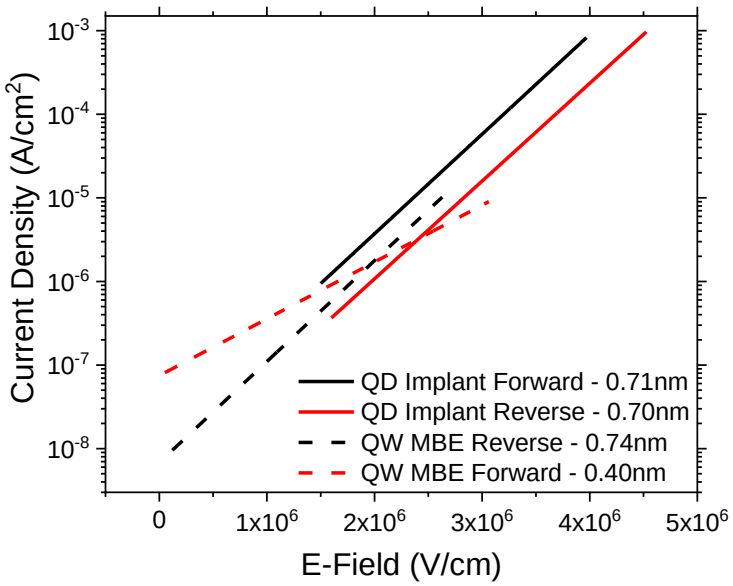

Figure 3.12: Graphical representation of the hopping conduction models of MBE grown Si QWs and ion implanted QDs in SiO_2

We observe a difference in forward and reverse biases where the trap spacing for forward biases is almost half the trap spacing of the reverse bias. This difference in trap spacing can be attributed to charge accumulation at trap sites, allowing for carriers to move more freely in one direction and not the other.

Following the model, the ion implanted samples showed a similar hopping trap site distance of around 0.73 ± 0.03 nm. Assuming a homogenous distribution of single sized quantum dots, a mean distance between quantum dots can be calculated via the following equation [14]

$$s = \left(\frac{2.9687 \times 10^7}{\sqrt[3]{C_{precipitate}}} - 1 \right) d \tag{3.5}$$

where $C_{precipitate}$ is the concentration of implanted Si in SiO_2 that precipitated into QDs. Taking an average size of 1.69nm QDs as seen in Mokry et al.[6] and PL measurements and using the precipitate concentration to be around 47% of the implant concentration from XPS results leads to a inter-QD distance of around 0.94nm. While slightly larger than the measured hopping distance, the true inter-QD value would be slightly lower, due to excess atomic Si in the SiO_2 matrix that would further lower the mean hopping distance to the interatomic distances of SiO_2.

Coulomb Blockade Effects

For small enough trap site systems, only a small finite number of charges can be stored within it. Once it is filled, a high enough E-field is required to emit that electron from the trap site. If the E-field is low, the coulombic effects at the trap site block other charges from moving through and the current is unable to rise, leading to a 'staircase-like' I-V curve. Coulomb blocking has previously been observed in single electron systems and quantum dots ensembles [20, 21]. We have observed Coulomb blocking effects, however the effects are not repeated at specific ΔV

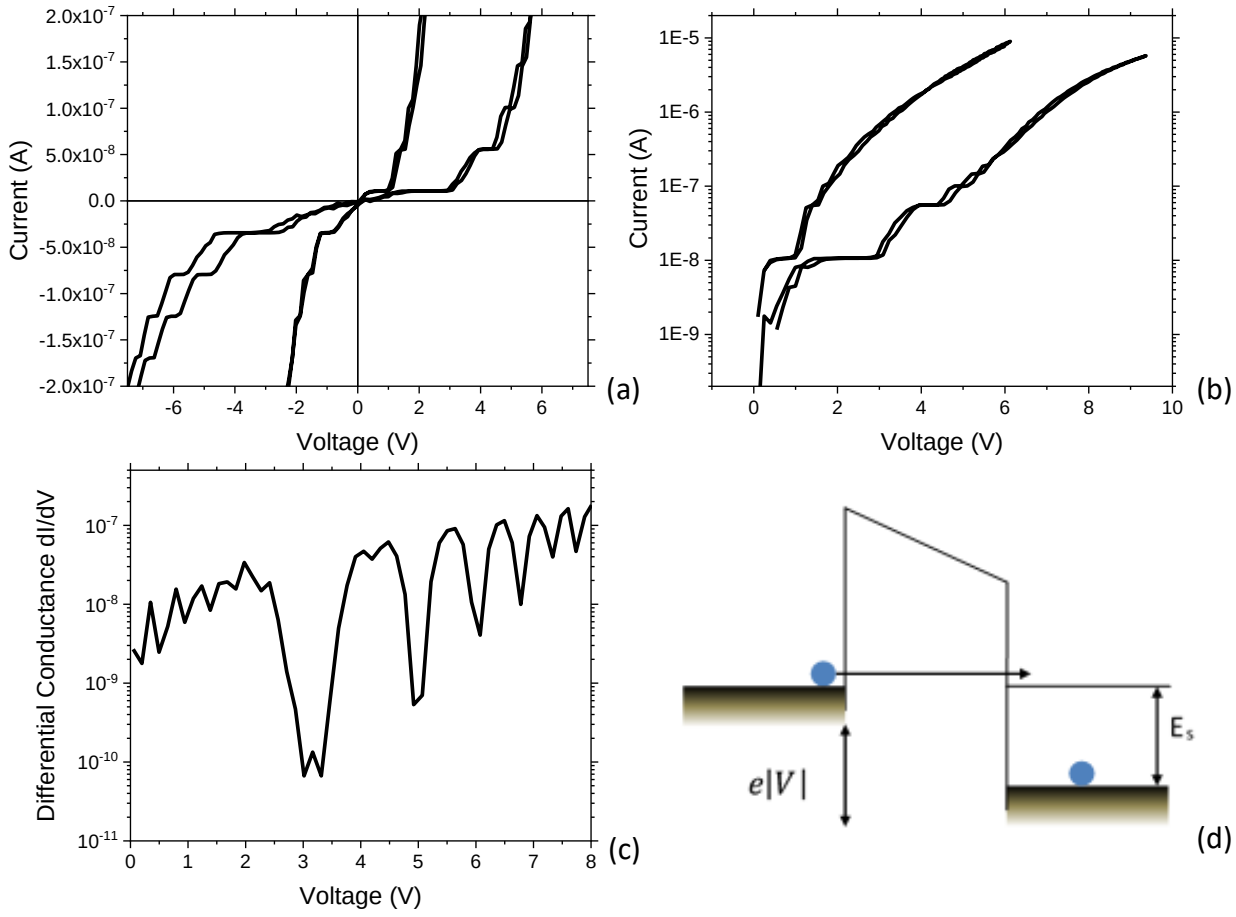

Figure 3.13: (a) Coulomb blocking effects for MBE grown Si QW samples for different Al pad pairs observed at nA scale. (b) Logarithmic currents for positive voltages only. (c) Differential conductance showcasing drops in conductance at specific voltages. (d) Band diagram showing CLB effect.

intervals. This shows that while there are quantum structures present in the sample, they are not as uniformly distributed as we expected them to be. Additionally, this random effect can be

attributed to the different traps present in the SiO_2 matrix, some of which could be attributed to the QW structure.

The ΔV width can be related to the capacitance of the quantum system as ΔV = e/C which can further be related to the size of the particle via the following equation [22, 23]

$$C = 4\pi\epsilon_r r\left[1 + \frac{r}{2l} + \frac{\left(\frac{r}{2l}\right)^2}{1 - \left(\frac{r}{2l}\right)^2}\right] \tag{3.6}$$

Where r is the size of the quantum structure and l is the thickness of the oxide. For an oxide thickness of 20nm and minimum measured ΔV ≈ 370mV, this leads to quantum dot size of ~1nm. However, there are a lot of ΔV intervals that are larger than 370mV and are not able to be accounted for. The ion implanted sample showed no signs of Coulomb blocking (CLB), we would expect to see CLB effects for samples with implantation energies low enough to have measurable direct tunneling, as we would expect to see more CLB effects at lower E-field strengths.

3.4. Conclusions

In section 1.3.2 of this thesis, different defect types were discussed. Seeing as 2 of our dominant charge transport mechanisms involve trap sites, further investigation into reconciling quantum dots and defects in the sample is warranted. Both samples showed Fowler-Nordheim and Poole-Frenkel emissions with model parameters showing good agreement to previous measurements of off-stoichiometric silicon oxide films. MBE grown QW samples showed direct tunneling due to the much thinner layer of SiO_2 compared to the implanted QD sample. In addition, the optical dielectric constant was able to be calculated as part of the Poole-Frenkel model and agreed to previously measured optical dielectric constants modelled via ellipsometry. The dependence on PF and hopping conduction shows that trap site hopping is a dominating effect. Both measurements gave a similar value of distances between trap sites for hopping conduction mechanism of around 0.7nm. For the Si-QD sample, only a fraction of implanted Si condensed to quantum dots during the annealing process. If we assumed 47% of the implanted Si condensed to QDs (taken via XPS) and an average QD size of 1.69nm, we would get an average trap spacing

of 0.94nm. However even for less condensed fractions of Si, there will be an excess of Si atoms in the matrix that account for the reduction of spacing between trap sites.

It should be noted that while the MOS models are large scale models that are unable to conclude that quantum dots are embedded in this system, coulomb blocking and photoluminescence observations in MBE and implanted sampled respectively show that there are quantum structures in these systems. Table 3.1 shows a lot of overlap between conduction through quantum dots and conduction of non-stoichiometric silicon oxide films, which has already been studied extensively. Understanding the physics behind excess Si influencing the bandgap and DOS will help in understanding conduction mechanisms of quantum dots in oxide films. Previous studies creating memory devices with non-stoichiometric oxide films can be used as a baseline for creating similar devices with quantum dot structures [24].

Sample Reference	% Si excess	x (Si_xO_2)	Φ_b (eV)	Refractive Index (n)
Nazban et al, 2020	2nm Si-QW	-	0.28 ± 0.10	2.71 ± 0.75
Nazban et al, 2020	10 %	1.36	0.69 ± 0.13	1.73 ± 0.15
DiMaria et al, 1983 [16]	13 %	-	0.40	≈ 2.74
DiMaria et al, 1983 [16]	6 %	-	0.60	≤ 1.73
Kruchinin et al, 2019 [18]	-	1.34	-	1.77

Table 3.1: Values of barrier height and refractive index as a function of silicon content. Refractive Index values in references were taken via ellipsometry while this study used Poole-Frenkel modelling

3.5. References

[1] D. Vanmaekelbergh, P. Liljeroth, Electron-conducting quantum dot solids: novel materials based on colloidal semiconductor nanocrystals, Chemical Society Reviews, 34 (2005) 299-312.

[2] A. Abdelal, Silicon Nanostructures Deposited by Molecular Beam Epitaxy on Silicon Oxide, Physics & Astronomy University of Western Ontario, 2017.

[3] A.P. Alivisatos, Semiconductor Clusters, Nanocrystals, and Quantum Dots, Science, 271 (1996) 933-937.

[4] J.F. Ziegler, M.D. Ziegler, J.P. Biersack, SRIM - The stopping and range of ions in matter (2010), SAO/NASA Astrophysics Data System (2010).

[5] T. Nishimura, Computer simulation program for medium-energy ion scattering and Rutherford backscattering spectrometry, Nuclear Instruments and Methods in Physics Research Section B: Beam Interactions with Materials and Atoms, 371 (2016) 97-100.

[6] C.R. Mokry, P.J. Simpson, A.P. Knights, Role of vacancy-type defects in the formation of silicon nanocrystals, Journal of Applied Physics, 105 (2009) 114301.

[7] E.G. Barbagiovanni, D.J. Lockwood, P.J. Simpson, L.V. Goncharova, Quantum confinement in Si and Ge nanostructures: theory and experiment., Applied Physics Reviews, (2014) 1(1), 011302.

[8] G. Ledoux, O. Guillois, D. Porterat, C. Reynaud, F. Huisken, B. Kohn, V. Paillard, Photoluminescence properties of silicon nanocrystals as a function of their size, Physical Review B, 62 (2000) 15942-15951.

[9] S. Adachi, Properties of Group-IV, III-V and II-VI Semiconductors, John Wiley & Sons, 2005.

[10] Y.K. Xu, S. Adachi, Multiple-peak structure in porous Si photoluminescence, Journal of Applied Physics, 107 (2010) 123520.

[11] R. Guerra, E. Degoli, S. Ossicini, Size, oxidation, and strain in small Si/SiO_2 nanocrystals, Physical Review B, 80 (2009) 155332.

[12] C. Delerue, G. Allan, C. Reynaud, O. Guillois, G. Ledoux, F. Huisken, Multiexponential photoluminescence decay in indirect-gap semiconductor nanocrystals, Physical Review B, 73 (2006) 235318.

[13] S. Godefroo, M. Hayne, M. Jivanescu, A. Stesmans, M. Zacharias, O.I. Lebedev, G. Van Tendeloo, V.V. Moshchalkov, Classification and control of the origin of photoluminescence from Si nanocrystals, (2008).

[14] X.D. Pi, O.H.Y. Zalloum, A.P. Knights, P. Mascher, P.J. Simpson, Electrical conduction of silicon oxide containing silicon quantum dots, Journal of Physics: Condensed Matter, 18 (2006) 9943-9950.

[15] F.C. Chiu, A review on conduction mechanisms in dielectric films, Advances in Materials Science and Engineering, 2014 (2014).

[16] D.J. DiMaria, D.W. Dong, C. Falcony, T.N. Theis, J.R. Kirtley, J.C. Tsang, D.R. Young, F.L. Pesavento, S.D. Brorson, Charge transport and trapping phenomena in off stoichiometric silicon dioxide films, Journal of Applied Physics, 54 (1983) 5801-5827.

[17] R. Angle, H. Talley, Electrical and charge storage characteristics of the tantalum oxide-silicon dioxide device, IEEE Transactions on Electron Devices, 25 (1978) 1277-1283.

[18] V.N. Kruchinin, T.V. Perevalov, G.N. Kamaev, S.V. Rykhlitskii, V.A. Gritsenko, Optical Properties of Nonstoichiometric Silicon Oxide SiO_x ($x < 2$), Optics and Spectroscopy, 127 (2019) 836-840.

[19] A. Luna-López, M. Aceves-Mijares, O. Malik, Optical and electrical properties of silicon rich oxide films for optical sensors, Sensors and Actuators A: Physical, 132 (2006) 278-282.

[20] D.V. Averin, K.K. Likharev, Coulomb blockade of single-electron tunneling, and coherent oscillations in small tunnel junctions, Journal of Low Temperature Physics, 62 (1986) 345-373.

[21] M.D. Efremov, G.N. Kamaev, V.A. Volodin, S.A. Arzhannikova, G.A. Kachurin, S.G. Cherkova, A.V. Kretinin, V.V. Malyutina-Bronskaya, D.V. Marin, Coulomb blockade of the conductivity of SiO_x films due to one-electron charging of a silicon quantum dot in a chain of electronic states, Semiconductors, 39 (2005) 910-916.

[22] C.-H. Cho, B.-H. Kim, S.-J. Park, Room-temperature Coulomb blockade effect in silicon quantum dots in silicon nitride films, Applied Physics Letters, 89 (2006) 013116.

[23] S.M. Goodnick, Transport in Nanostructures, Nanoelectronics and Photonics, Springer, 2008, pp. 115-169.

[24] D.J. DiMaria, D.W. Dong, F.L. Pesavento, C. Lam, S.D. Brorson, Enhanced conduction and minimized charge trapping in electrically alterable read only memories using off stoichiometric silicon dioxide films, Journal of Applied Physics, 55 (1984) 3000-3019.

Chapter 4

4. Surface Debye temperature as a probe for epitaxial thin film defects

4.1. Introduction

Following the idea that the excess Si is a primary contributor to oxide conduction mechanisms with embedded Si quantum structures, a conclusion can be drawn on conduction via point defects and associated trap sites within the oxide layer. Understanding the nature of defects and being able to engineer defects is a useful tool in both academic studies and industrial applications and is the focus of this chapter. Additionally, conduction processes such as the Mott-Davis small-polaron hopping mechanism require measurements of the Debye temperature to be accurately modeled [1]. Defect densities were studied via RBS and the Debye temperature was estimated via LEED. Confirming the correlation between Debye Temperature measured via LEED and defects measured via RBS allows one to use LEED to monitor the creation and propagation of defects during crystal growth processes.

The Debye model estimates the contribution of phonons within a crystalline lattice of a material to the specific heat of the material. Accordingly, the Debye temperature (θ_D) of a solid is the temperature representation of all phonons vibrating with the highest normal mode of vibration and is a representation of the elasticity and stiffness of the bonds between its constituent atoms. The under-coordinated surface atoms of a solid tend to be more loosely bound and more energetic than their bulk counterparts [2, 3]. The Debye temperature tends to decrease in the vicinity of the surface such that the end point value found for the top atomic layer is known as the surface Debye temperature. The impact of the surface θ_D is significant. The increased vibrational amplitude at the surface, due to the lower surface Debye temperature, can allow for the melting of a solid from the surface inward in some materials [2], even if the temperature is below the bulk melting temperature. An important interconnected phenomenon is the presence of defects in the surface and near-surface layers. Interpretation of surface θ_D is even more complex in the presence of defects [4], motivating research to develop new tools to study defects and their contribution to the surface Debye temperature [5].

The Debye temperature of bulk materials has been measured using various experimental techniques, including x-ray diffraction [6, 7], helium atom scattering [8, 9], reflection high energy positron diffraction [10], ultraviolet photoemission spectroscopy [11], and Mossbauer spectroscopy [12]. The ability of such techniques to measure the true surface Debye temperature, rather than the bulk or a combination of the surface and bulk, depends obviously on their surface specificity. Some techniques, such as XRD when combined with Rietveld refinement, have the advantage of elemental specificity and are able to assign a Debye temperature to each element in the structure. In the case of ^{57}Fe Mossbauer spectroscopy on $Fe_{0.01}Cr_{99.9}$ [12], it has been noted that the effective θ_D that is measured is only representative of the Fe impurities which have become uncoupled from the Cr lattice.

This research is aimed to look at the potential of using low energy electron diffraction (LEED) to quantify surface Debye temperature for several semiconductor materials important for optoelectronics, photonics and other thin film applications. Low energy electron diffraction (LEED) uses the constructive interference of a mono-energetic beam of electrons, with typical energies of 50-200eV that have been scattered off a crystalline surface to measure the interatomic distances and thus elucidate the surface structure. LEED diffraction patterns can be fitted to models based on dynamical LEED theory – which takes into account multiple scattering events. This is a more demanding but analogous process to the Rietveld refinement which can also allow a Debye temperature to be assigned to individual elements in a multi-element alloy or compound [13]. There have also been efforts in the past to determine surface θ_D [8, 9] by LEED complemented by theoretical approaches [13, 14].

Rutherford Backscattering Spectroscopy has often been used in the past to probe defects in crystal structures using its ion channeling phenomenon [15], as described in chapter 2. Accelerated ions (typically He^{2+}) bombard the sample, with the detector mounted at a scattering angle of 170º to the incident beam. This allows for detection of ions that are backscattered from elastic collisions with the nucleus. For the sample orientation that matches the orientation of the crystalline lattice to the direction of the ion beam, the ions can pass through a sizeable portion of the material. While random oscillations can still cause a low backscatter signal that increases with depth, the majority of backscatter signal in channeling mode is due to imperfections in the crystalline matrix. For single crystal structures this would be due to interstitial defects. Structures

with multiple layers would have an increase in visibility at the layer interface due to stress of the lattice structure near the interface.

4.2. Experimental Details

Several different samples pertaining to Si and Ge crystal structures were studied in this project. 1μm and 0.6μm Si epitaxial films on sapphire (SOS) are commercially available samples fabricated via hetero-epitaxial growth on Al_2O_3 $(\bar{1}102)$ substrates, the sapphire samples are oriented along the R-plane. Epitaxially grown 0.5μm Ge /Si (100) was used to study the defect structures of layers that share the same crystallographic structure with different lattice constants (a_{Si}=5.431 Å, a_{Ge}=5.658 Å). Single crystal samples of p-type Si (100) (1-10 Ω/cm), n-type Ge (100) (> 50 Ω/cm) and Al_2O_3 $(\bar{1}102)$ were used as references. This allows us to study the effect of epitaxial film thickness and to study defect relaxation towards the surface. Standard HF-etching procedures for the removal of the surface oxide were applied for the Si (001) surfaces prior to all analyses. Typical dimensions of the samples were 10×10×0.5 mm.

Rutherford backscattering spectroscopy (RBS) was applied to probe elemental depth profiles for all samples in random and channeling geometry, using 2.0 MeV He^+ ions produced by the 1.7 MV Tandetron facility with a Si detector positioned at a scattering angle of 170°. For random geometry spectra, samples were continuously rotated around the azimuth with a tilt angle of 5° during data acquisition to avoid channeling. For channeling geometry, samples were aligned to the [001] crystallographic direction in order to quantify the number of atoms in the crystalline lattice that were displaced from their ideal lattice sites. An initial calibration with Sb-implanted Si and diamond-like carbon standards were used to precisely calibrate peaks after which RBS spectra can be simulated and matched to the data. The uncertainty of ion yields obtained by RBS measurements derived from this standard is close to 3.5%. Sb areal density is estimated with an accuracy of approximately 2.2%. SIMNRA and MEISwin software were used to simulate RBS spectra.

A low energy electron diffraction (LEED) instrument incorporating a position-sensitive pulse - counting detector with high bias current microchannel plates was used to rapidly collect digital LEED images with low total electron exposure. Details related to this system were published elsewhere. [reference previous paper on the LEED system here]. In order to calculate surface θ_D,

first we used MultLEED software to zoom in on the peak of interest. Next, the sample was heated using an e-beam heater installed behind the sample to 700-800^{o}C within a few seconds. Then, the intensity of the diffraction peak *I* was recorded as the sample was cooled to room temperature. The theoretical basis for the Debye temperature calculation is given in the next section.

4.3. Theory of Debye temperature calculations from LEED

The Debye temperature, $\theta_{D,}$ is calculated using a set of equations which connect the Debye-Waller factor, W, and the intensity of one of the diffraction peaks from an electron beam incident on a crystal [2]. By analogy with x-ray diffraction, we can assume that the elastic intensities are reduced by the Debye-Waller (DW) factor, designated as *W* below:

$$I - I_{bk} = I_0 e^{-2W} \tag{4.1}$$

$$2W = \frac{24 m_e (E cos^2\alpha + V_0) T}{m_a k (\theta_D)^2} \tag{4.2}$$

where *2W* is the Debye-Waller factor, m_e is the mass of the electron, *E* is the electron energy, α is the angle of incidence, V_0 is the inner potential of the crystal, *T* is the temperature of the sample during measurement, m_a is the mass of the atoms in the crystal, *k* is Boltzmann's constant, θ_D is the Debye temperature, *I* is the diffracted LEED spot intensity, I_{bk} is the background intensity, and I_0 is the incident electron beam intensity. One can rearrange Equations 4.1 and 4.2 to be of the form:

$$\ln \frac{I - I_{bk}}{I_0} = -\frac{24 m_e (E cos^2\alpha + V_0)}{m_a k (\theta_D)^2} T \tag{4.3}$$

plotting $\ln \frac{I - I_{bk}}{I_0}$ vs T and calculating the *slope* of the line allows the Debye temperature, $\theta_{D,}$ to be found from equation 4.4:

$$\theta_D = \sqrt{-\frac{24m_e(Ecos^2\alpha + V_0)}{m_a k \times Slope}} \quad (4.4)$$

4.4. Experimental results and discussion

4.4.1. Defects in Si: RBS

Figure 4.1a shows the RBS spectrum obtained from a Si (001) wafer with the native SiO_2 layer removed prior to analysis. Scattering yields for the sample aligned in the [001] direction are compared to "random" geometry spectrum. Single crystal Si(100) shows mostly scattering from disordered surface layers, with a surface peak at 1130 keV and with very low scattering yield below the surface corresponding to a little defect presence. When a highly collimated beam of ions is directed at a crystalline target along a direction of high symmetry, deflection of the incident ions from the atoms along a row parallel to the beam leads to the formation of a shadow cone, therefore reducing the probability of scattering from lattice atoms located deeper within the crystal. In the channeling geometry, the majority of elastically scattered ions cannot be scattered until they collide with interstitial atom, resulting in a small angle deflection.

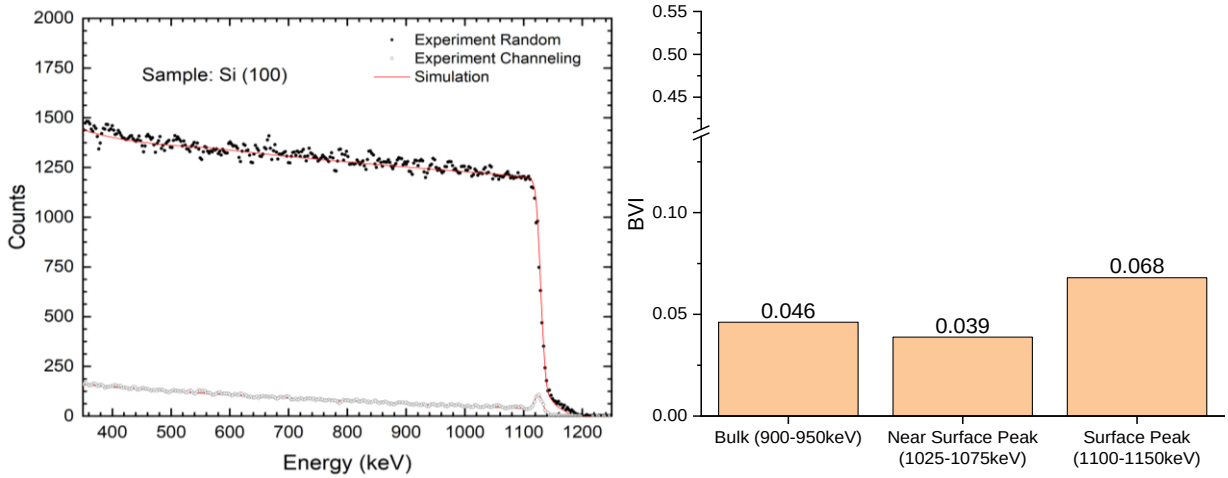

Figure 4.1: (a) RBS spectra for incident 2.0 MeV He^+ for Si (100) taken at both random rotating and channeling geometries. Intensity simulated by SIMNRA is shown for the random geometry spectrum (red line). (b) BVI values for Si (100) showing an increase in defects at the surface peak. Relative uncertainties of the presented BVI factors are close to 3.5%.

In order to quantify interstitial defects in a sample by RBS, we introduce the beam visibility index (BVI) defined as:

$$BVI = \frac{\int_{E_1}^{E_2}(Channeling\ Curve)dE}{\int_{E_1}^{E_2}(Random\ Curve)dE} \quad (4.5)$$

with its value scaling proportionally with defect concentrations from 0 to 1. Since the random ion yields is taken to be the maximum possible counts (all atoms visible), a lower channeling yields indicates fewer defects and a lower BVI, while a higher yield indicates higher defect amounts with a higher BVI.

Three thin layers of the same physical thickness and corresponding energy width $\Delta E = E_2 - E_1$ were selected within the sample to monitor the defect concentrations for those regions. First, a top surface layer (1100-1150 keV) corresponds to the surface peak of the RBS (with usually higher defect concentration than the bulk due to surface termination and disorder). Second, a near-surface layer (1025-1075 keV) was selected right below the surface layer, and finally, a thin layer corresponding to the bulk Si (900-950 keV) was analyzed, this energy range is corresponding to ~500 nm below the surface.

Note that ion scattering yield increases as we probe deeper into the sample at lower energies, due to multiple scattering, and while defect concentrations stay constant, we see a small increase in BVI. As we probe deeper in RBS measurements, the ions have an increase in the probability of having undergone collisions, which leads to a systematic increase of ion yield with depth. Assuming that the Si (001) single crystal has constant defect density in its bulk, we can make a correction for BVI to keep it constant with depth.

$$\Delta BVI_{Si}\ \alpha = (8.21\ \times 10^{-5})\ \times \Delta Energy\ (keV) \quad (4.6)$$

This correction is sensitive to a material type. All calculated BVI parameters are summarized in Table C.1 for Si and Ge. Different BVI corrections can be calculated from other bulk materials, where the defect density remains constant throughout the bulk.

Figure 4.2 presents RBS spectra for 1μm thick epitaxially-grown Si on sapphire, along with calculated BVI values. Similar measurements were obtained for a 0.6μm thick film (Appendix C, Figure C.1). Comparing the two Si films on sapphire, we observe that the film defect

concentration is highest near the Si/Al_2O_3 interface and decreases closer to the top surface. Energy intervals for BVI calculations were selected to be constant between the two samples to ensure we can compare the two BVI values for relatively similar surface and near surface layers. The thinner 0.6μm sample shows a higher defect concentration than the 1μm sample at their respective surface layers. This difference is consistent with the Debye temperatures from the top surface, calculated from LEED measurements.

Note that the Si thin films samples are not thick enough to reduce the defects to the level of a bulk Si (100) wafer. A thicker sample would reduce the lattice stress, and consequently defect concentration, to the point of Si(100). The BVI factor for the1μm sample for the Si/Al_2O_3 interface (0.52 ±0.03) shows a slight increase of defect concentration at the interface compared to the 0.6μm sample (BVI = 0.48±0.03). However, this difference can be argued to be insignificant within experimental uncertainties, including (a) RBS ion yield measurements, and (b) the systematic increase in BVI with depth. Applying the depth correction from Si (100) to the 0.6μm Si sample gives us a BVI of 0.50 ±0.02 at a depth of 1μm. The discrepancy can be attributed to the change of slope in counts at the interface layer.

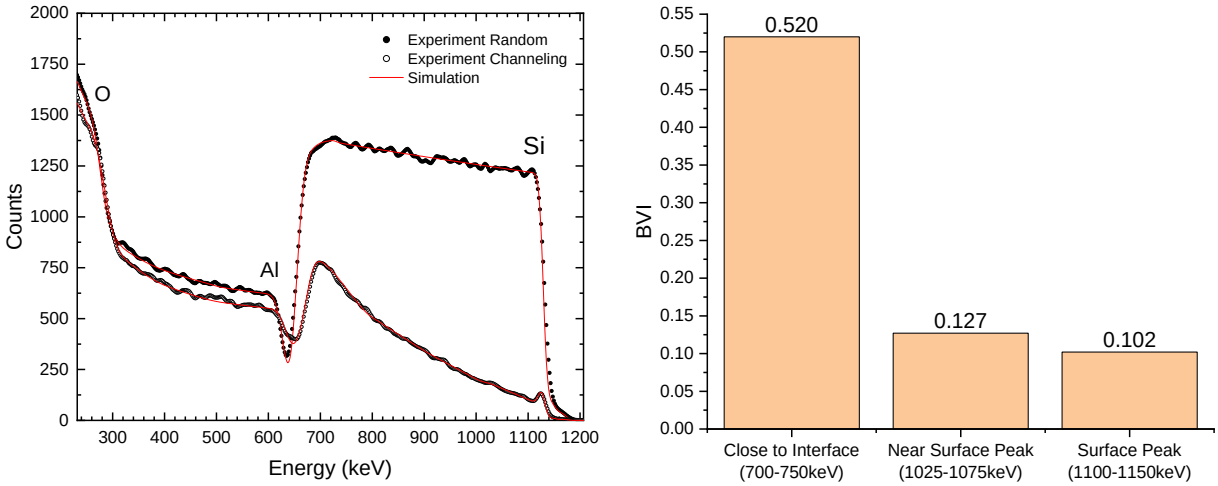

Figure 4.2: (a) RBS spectra of 1μm grown Si on sapphire taken at both random and channeling geometries. (b) BVI values showing an increase in defects closer to the interface.

4.4.2. Defects in Ge: RBS

RBS spectra from a 0.5 μm epitaxial Ge film on Si (001) are presented in Figure 4.3, along with calculated BVI values. Notice that Ge atomic number is larger, and so it is detected at higher energies in RBS, for the same incident energy, and it has a larger scattering cross section than Si. Similar to Si(100), Ge(100) shows a very small defect concentration with a slight increase at the surface (see Appendix C, Figure C.2)

2). A similar increase in BVI is observed with depth due to the increased probability of collisions with atoms in the Ge bulk. A correction factor is calculated to be

$$\Delta BVI_{Ge}\ \alpha = (3.55\ \times 10^{-4})\ \times \Delta Energy\ (keV) \qquad (4.5)$$

The higher correction factor is expected since heavier elements will have larger correction factors.

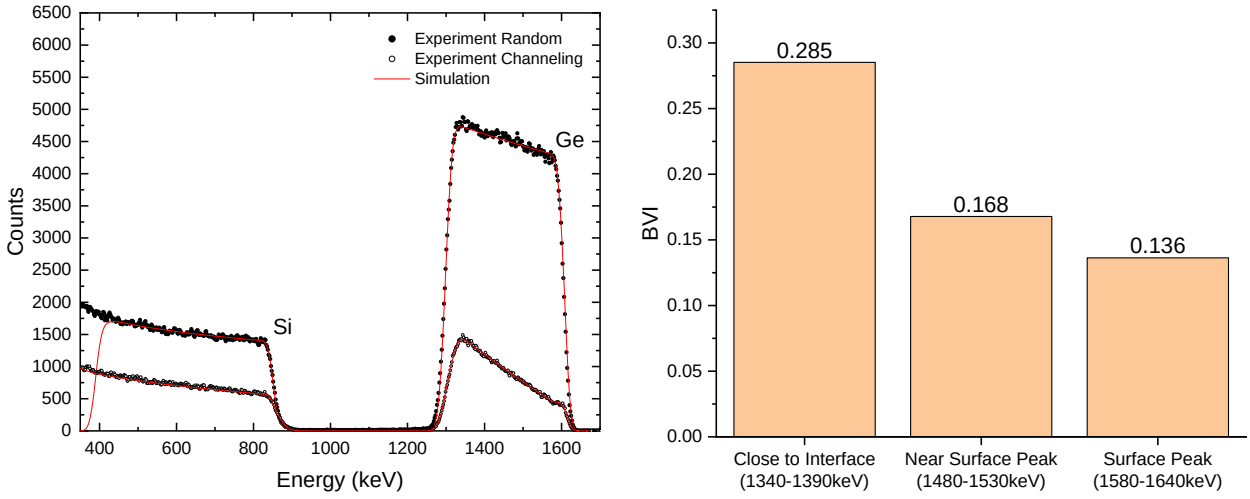

Figure 4.3: (a) RBS Spectra of 0.6μm grown Ge on Si (001) taken at both random rotating and channeling geometries. (b) BVI values showing an increase in defects closer to the interface.

The surface peak for Ge is close to 1600 keV. Note that the calculated BVI factor for Ge may be slightly higher compared to Si (001), as no etching was used to remove the small amount of Ge oxide on the surface. Notably, the BVI associated with the Ge/Si (001) interface is significantly smaller for Ge compared to Si/Al_2O_3 (SOS) films. Since the crystal structures of Si and Ge are both diamond-like $F_D\overline{3}_M$ structures, the main cause for defects would be the different lattice constants (5.658Å for Ge vs 5.4307Å for Si). Reduction of BVI values from the interface to the

near-surface layer and finally to the surface can be connected to a gradual reduction of strain in the epitaxial film.

Surface BVI factors for Si and Ge will be compared to the surface Debye temperatures, measured by LEED, in the following section.

4.5. LEED for Debye temperature: Si and Ge

A Representative LEED diffraction pattern for the Si (001) surface at room temperature is shown in Figure 4.4 (a). The experimental methodology applied for calculating Debye temperatures for different Si (001), Ge (001) and Si and Ge epi- thin film surfaces has been summarized in section 4.3. Besides the usual visual inspection of the diffraction pattern with a fluorescent screen, this instrument allows direct quantitative determination of the electron intensity distribution. For this purpose, we can focus on one of the diffraction spots and measure the beam intensity with a position sensitive detector/multichannel plate combination. Here we would like to note that the choice of LEED spot to use in the calculation of Debye temperature has a large effect on the final results. Attempts to correlate the disparity between spots on the same image with distance from the (00) diffraction spot showed no correlation. We also found some relationship to the incident electron beam energy. Typical beam energies used were between 70 and 200 eV.

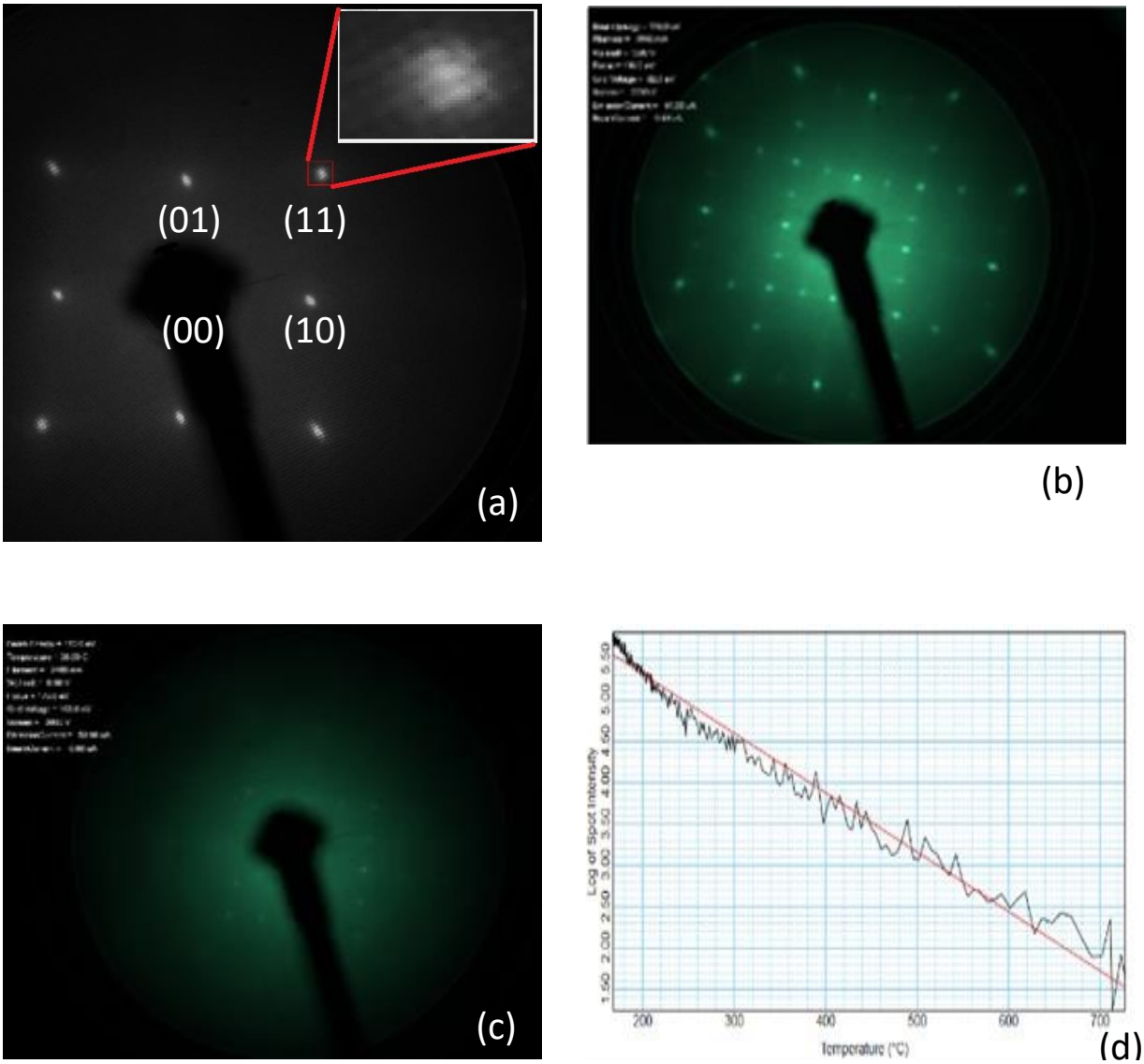

Figure 4.4: (a) Typical LEED image from MultLEED software at 240ºC with enlarged diffraction peak used for Debye temperature analysis, shown in an inset. Incident electron beam energy = 120eV. Screen voltage = 3.0keV, emission current 42 mA. Diffraction peak indices are provided with (00) peak being obstructed by electron gun shadow. (b) LEED diffraction pattern for Si (100) at 850ºC, (c) LEED pattern for Si(100) at final measured temperature, close to room temperature, (d) Plot of ln(*I*) vs T, showing a best linear fit for calculating Debye temperature.

Table 1 summarizes representative BVI values for the surface peaks, calculated from RBS results, along with Debye temperatures for the same surfaces for two different energies. From comparison of BVI factors from RBS results, between two epitaxial Si films, the thinner 0.6μm sample has a higher defect concentration near the surface than the 1μm sample. This difference is

consistent with the Debye temperatures from the top surface, calculated from LEED measurements.

Sample	**Surface BVI for top 0-5nm**	**LEED (θ_D), K at 95 eV**	**LEED (θ_D), K at 150 eV**	**Bulk θ_D** [16]
Si (001)	0.068 ± 0.002	608	621	645
1 μm SOS (Si/Al_2O_3)	0.102 ± 0.004	574	585	
0.6μm SOS (Si/Al_2O_3)	0.195 ± 0.004	535	547	
Ge (001)	0.132 ± 0.005	398*	413**	374
1 μm Ge/Si (100)	0.136 ± 0.005	419*	402**	

Table 4.1: Beam visibility index (BVI) from RBS and measured Debye temperatures (θ_D) from LEED compared to published results for Si (001) and Ge (001). *LEED pattern was acquired at 100eV; **LEED pattern was acquired at 145eV.

Additionally, the inclusion of the inner potential creates difficulty, as not all crystalline substances have recorded inner potentials. Calculating the inner potential is complex and yields results which can vary widely depending on what assumptions are made. Experimental determination of the inner potentials is impractical for the purposes of Debye-LEED. For the first iteration of the calculation software the inner potential was assumed to be 15 V since this value is roughly the mean of values which could be found in the literature and does not affect the value of θ_D as strongly as the $E\ cos^2\ \alpha$ term.

Also, the calculation software does not allow for specification of the angle of incidence or the mass of the atoms in the crystal. These parameters are necessary to obtain an accurate Debye temperature estimate. In addition to this, the treatment of m_a in the case of a crystal with more than one element is unclear in the source material for the equation.

4.6. Conclusions

In this project, we have used a suite of near-surface characterization techniques to characterize and quantify defects on the surface and in the near-surface region of epi-films compared to single crystals. We applied Rutherford backscattering spectroscopy (RBS, random and channeling), and low energy electron diffraction (LEED) to quantify defect density and distribution in several epitaxially grown thin films. Our experimental results derived from LEED diffraction patterns for Si and Ge surfaces showed θ_D values lower than the bulk temperatures. However, experimental uncertainties associated with Debye LEED calculations are large, and show strong dependence on the diffraction peak index, incident electron energy, and inner potential values used in calculations. We found good agreement between estimates of surface $\theta_{D,}$ from LEED, and BVI values from RBS, as an indicator of defect density on the surface of Si and Ge epitaxial films. Typically, lower surface Debye temperatures are measured for epitaxial films that exhibit a larger number of defects. Using RBS, we have applied a new methodology to measure and quantify interstitial defect concentration as a function of depth in Si and Ge epitaxial films on single crystal substrates.

4.7. References

[1] N.F. Mott, E.A. Davis, Electronic processes in non-crystalline materials, Oxford university press, 2012.

[2] J.T. Yates, Experimental Innovations in Surface Science: A Guide to Practical Laboratory Methods and Instruments, Springer-Verlag, New York, 1998.

[3] M.A. VanHove, W.H. Weinberg, C.-M. Chan, Low-Energy Electron Diffraction: Experiment, Theory, and Surface Structure Determination, Springer verlag, Berlin, 1986.

[4] J. Spitaler, S.K. Estreicher, Perspectives on the Theory of Defects, Front. Mater., 5 (2018) 17.

[5] M. Henzler, LEED Studies on Surface Imperfections, Applied Surface Science, 11/12 (1982) 450-469.

[6] M. Chollet, J. Lechelle, R.C. Belin, J.C. Richaud, In situ X-ray diffraction study of point defects in neptunium dioxide at elevated temperature, J. Appl. Cryst., 47 (2014) 1008.

[7] C. Young, J. Petrosky, J.M. Mann, E.M. Hunt, D. Turner, P.A. Dowben, The lattice stiffening transition UO_2 single crystals, J. Phys.: Condens. Matter, 29 (2017) 035005.

[8] W. Steurer, A. Apfolter, M. Koch, W.E. Ernst, B. Holst, Surface Debye temperature of alpha-quartz (0001), Surface Science, 602 (2008) 1080.

[9] A. Tamtogl, M. Mayrhofer-Reinhartshuber, P. Kraus, W.E. Ernst, Surface Debye temperature and vibrational dynamics of Antimony(111) from helium atom scattering measurements, Surface Science, 617 (2013) 225.

[10] Y. Fukaya, A. Kawasuso, K. Hayashi, A. Ichimiya, Precise determination of the surface Debye-temperatureof Si(111)-7 x 7 surface by reflection high-energy positron diffraction, Applied Surface Science, 237 (2004) 29.

[11] C. Waldfried, D.N. McIlroy, J. Zhang, P.A. Dowben, G.A. Katrich, E.W. Plummer, Determination of the surface Debye temperature of Mo(112) using valence band photoemission, Surface Science, 363 (1996) 296.

[12] S.M. Dubiel, J. Cieslak, B.F.O. Costa, Debye temperature of disordered bcc-Fe-Cr alloys, J. Phys.: Condens. Matter, 22 (2009) 055402.

[13] E.A. Soares, V.E. de Carvalho, V.B. Nascimento, A layer-by-layer study of CdTe(110) surface Debye temperature and thermal vibrations by low energy electron diffraction, Surface Science, 431 (1999) 74.

[14] D.P. Jackson, Approximate calculation of surface Debye temperatures, Surface Science, 43 (1974) 431-440.

[15] E. Albertazzi, M. Bianconi, G. Lulli, R. Nipoti, M. Cantiano, Different methods for the determination of damage profiles in Si from RBS-channeling spectra: a comparison, Nuclear Instruments and Methods in Physics Research Section B: Beam Interactions with Materials and Atoms, 118 (1996) 128-132.

[16] C. Kittel, Introduction to Solid State Physics, New York: John Wiley, 1986, pp. 185.

Chapter 5

5.1. Conclusions

The goal of this thesis is to better understand and model electrical processes of quantum structures made via solid state fabrication processes. In Chapter 3, two different solid-state fabrication processes were described, molecular beam epitaxy (MBE) and ion implantation, to fabricate Si Quantum Wells and Si Quantum Dots, both systems embedded in an SiO_2 matrix, respectively. Depth analysis using Rutherford Backscattering quantitatively confirmed the distribution of Si as a function of depth. These RBS results complemented by X-ray photoelectron spectroscopy (XPS), scanning electron microscopy (SEM) and high resolution transmission electron microscopy (HRTEM) have given us confirmation of Si QWs and Si QDs in each system of samples.

Photoluminescence measurements were performed on the Si quantum structure samples. While the MBE grown Si-QW samples showed no measurable photoluminescence, the implanted Si-QDs sample gave a multi peak spectrum with a maximum at around 760nm (1.62eV) corresponding to a mean QD size of 1.69nm, which closely matches the mean QD diameter estimated in a previous study by Mokry et al., also prepared in our group by ion implantation at the Tandetron facility at the University of Western Ontario [1]. Furthermore, the PL spectrum edges showed strong asymmetry and the spectrum has several just resolvable peaks with a separation of approximately 62meV. The Configurational-Coordinate (CC) model has been used in the past to explain this multi-peak phenomenon where the vibrational energy levels within the band structure are separated by the long wavelength optical phonon frequency corresponding to 64meV for silicon [2]. Deconvolution of the spectrum with a 62meV separation made a precise fit, however this resulted in fitting the spectrum with a minimum of 4 peaks or more, leading to a case of overparameterization in the model. Other possible causes of these peaks could be defect structures caused by the ion implantation process. However, since the final step of the process involved two annealing procedures including hydrogen passivation, this is considered less likely.

Previously, XPS measurements taken by Barbagiovanni et al. [3] gave an understanding of the interface region and amount of QDs in the sample. The ratio of Si (0) to Si (IV) oxidation state is

used to calculate the fraction of Si that condensed into QDs which was estimated to be 47 ± 5% of the implant dosage. Additionally, the ratio of XPS peaks, corresponding to the sum of Si(II) and Si(III) oxidation states, to the Si(0) state is estimated at 29%. This is slightly larger than a single interface layer of Si atoms around a Si QD of a size of 1.62nm (3x3x3 Si cubic unit cells) which is estimated to be 18.3% of the Si QD weight. Hence some of the Si(II) and Si(III) states can be attributed to both interstitial atoms in the SiO_2 matrix and atoms at the Si/SiO_2 interface, contributing to the defect density in SiO_2.

Both groups of samples - MBE grown Si-QW structures and implanted Si-QD structures - had their electrical characteristics probed. All samples had 100nm thick Al contact probes, with similar but not identical geometry on each sample. Both groups of samples showed Fowler-Nordheim and Poole-Frenkel emissions with model parameters showing good agreement to previous measurements of non-stoichiometric silicon oxide films. MBE grown QW samples showed direct tunneling due to the much thinner layer of SiO_2 compared to the implanted QD sample and high conductivity due to the nature of the sample with barrier heights of 0.3eV and 0.7eV in the QW and QD structures, respectively. In addition, the optical dielectric constant was calculated as part of the Poole-Frenkel model to be 2.71 for the QW and 1.73 for the QD samples which agree to previously measured optical dielectric constants of non-stoichiometric SiO_2 modelled via ellipsometry [4, 5]. Both measurements gave a similar value of distances between trap sites for hopping conduction mechanism of around 0.7nm. For the Si-QD sample, only a fraction of implanted Si condensed to quantum dots during the annealing process. Assuming 47% of the implanted Si condensed to QDs (via XPS) and an average QD size of 1.67nm (via TEM), we would get an average trap spacing of 0.94nm. However even for less condensed fractions of Si, there will be an excess of Si atoms in the matrix can account for the reduction of spacing between trap sites. Additionally, the Si-QW structures showed signs of coulomb blockade, albeit with random intervals of ΔV. This shows that while there are quantum structures present in the sample, they are not as uniformly distributed as we expected them to be. The Si-QDs showed no signs of coulomb blockade. CLB effects could potentially be measured for ion implanted samples at lower energies that result in QDs closer to the surface and with a higher density.

As defect structures are important in the transport and optical mechanisms of Si QDs in SiO_2, we show a way to analyze defect structures using both RBS and LEED. Defect structures in

commercially prepared samples of Si and Ge were analyzed using LEED measurements. The change in LEED pattern intensity vs temperature allows us to model the sample with the Debye temperature as a parameter. This allows our industrial collaborator (OCI), a manufacturer of LEED and MBE instruments, to study defects in a sample by outputting a single parameter characterizing the defect density of the sample. Commercially prepared Si (100) and two Si on sapphire (SOS) samples (0.6um and 1um each) were used to study how the defect structure is affected by the different fabrication processes and sample specifications. LEED patterns at 195eV show a definitive decrease in Debye temperature with increase in defects at the surface layer. However the choice of LEED diffraction spot for measurements can change the results, leading to large errors on this measurement. The sample interstitial defect density was verified via RBS channeling. The BVI parameter was introduced as a method of quantifying the defect structure measured via RBS. This value was taken as the ratio of channeling to random counts for a specified interval of energy. Results were used to compare to Debye temperature measurements from LEED and show general qualitative between the two methods.

5.2. Future plans and closing statements

With regard to electrical conduction, better separation between Fowler-Nordheim and Poole-Frenkel models can be achieved via temperature dependent electrical measurements. The Poole-Frenkel effect is expected to contribute less at lower temperatures, since thermionic effects are the driving factor behind the process, while Fowler-Nordheim should still be present, allowing a better separation between these models as they both came into effect at a similar electric field strength at room temperature. A temperature dependent electrical study will also allow us to model the PF effect with an Arrhenius plot, with J/E vs 1/T, allowing us to estimate a trap level that would have a temperature dependance on the Poole-Frenkel effect. Additionally, more accurate hopping range models such as the Mott-Davis variable-range hopping model (VRH) and small-polaron hopping model (SPH) can be determined via temperature dependent electrical measurements, as the hopping mechanism described in Chapter 3 is an approximation of hopping between point sources, and cannot distinguish between hopping via Si-QDs or hopping via Si-interstitials.

Another experiment that can be done would be to use time resolved photoluminescence (TRPL) to verify the lifetimes of the recombination process for the QD sample. This would allow better

understanding of the causes of photoluminescence as we expect different magnitudes of lifetimes for luminescence at the interface (due to defect structures) compared to the luminescence from the Si QDs themselves. Additionally, probing PL in the NIR (Near Infra-Red) wavelengths may show more defect associated luminescence. In addition, an annealing process in forming gas (95% N_2, 5% H_2) can be done on the MBE sample to reduce the number of defects causing non-radiative recombination effects, potentially increasing the PL yield to a measurable value.

Combining the conclusions made from chapters 3 and 4, previously prepared annealed ion implanted samples or MBE samples can be bombarded with a range of low energy ion dosages to create defects in the sample that are correspondingly measured via LEED. Probing the electrical and optical characteristics of these samples will allow us to model the transport properties of the sample more conclusively with regards to density of defects and conduction via trap sites such as Poole-Frenkel and hopping conduction mechanisms. However, this will limit measurements that are sensitive to the Si-QDs such as coulomb blocking effects and PL measurements.

This thesis has given a baseline on the optical and electrical properties of solid-state fabricated Si quantum structures in SiO_2. There is still much work that needs to be done in understanding the translation of electrical and optical signals. Once the current electrical and optical models are better understood independent of each other, the next step would be to look at electroluminescence and photovoltaic applications of these Si quantum structures in SiO_2 to better understand how optical and electrical signals can be translated, allowing us to build devices in the future that could do just that.

5.3. References

[1] C.R. Mokry, P.J. Simpson, A.P. Knights, Role of vacancy-type defects in the formation of silicon nanocrystals, Journal of Applied Physics, 105 (2009) 114301.

[2] Y.K. Xu, S. Adachi, Multiple-peak structure in porous Si photoluminescence, Journal of Applied Physics, 107 (2010) 123520.

[3] E.G. Barbagiovanni, D.J. Lockwood, P.J. Simpson, L.V. Goncharova, Quantum confinement in Si and Ge nanostructures, Journal of Applied Physics, DOI (2012) 111(113), 034307.

[4] D.J. DiMaria, D.W. Dong, C. Falcony, T.N. Theis, J.R. Kirtley, J.C. Tsang, D.R. Young, F.L. Pesavento, S.D. Brorson, Charge transport and trapping phenomena in off stoichiometric silicon dioxide films, Journal of Applied Physics, 54 (1983) 5801-5827.

[5] V.N. Kruchinin, T.V. Perevalov, G.N. Kamaev, S.V. Rykhlitskii, V.A. Gritsenko, Optical Properties of Nonstoichiometric Silicon Oxide SiO_x ($x < 2$), Optics and Spectroscopy, 127 (2019) 836-840.

Appendix A – Chapter 2 Supplementary

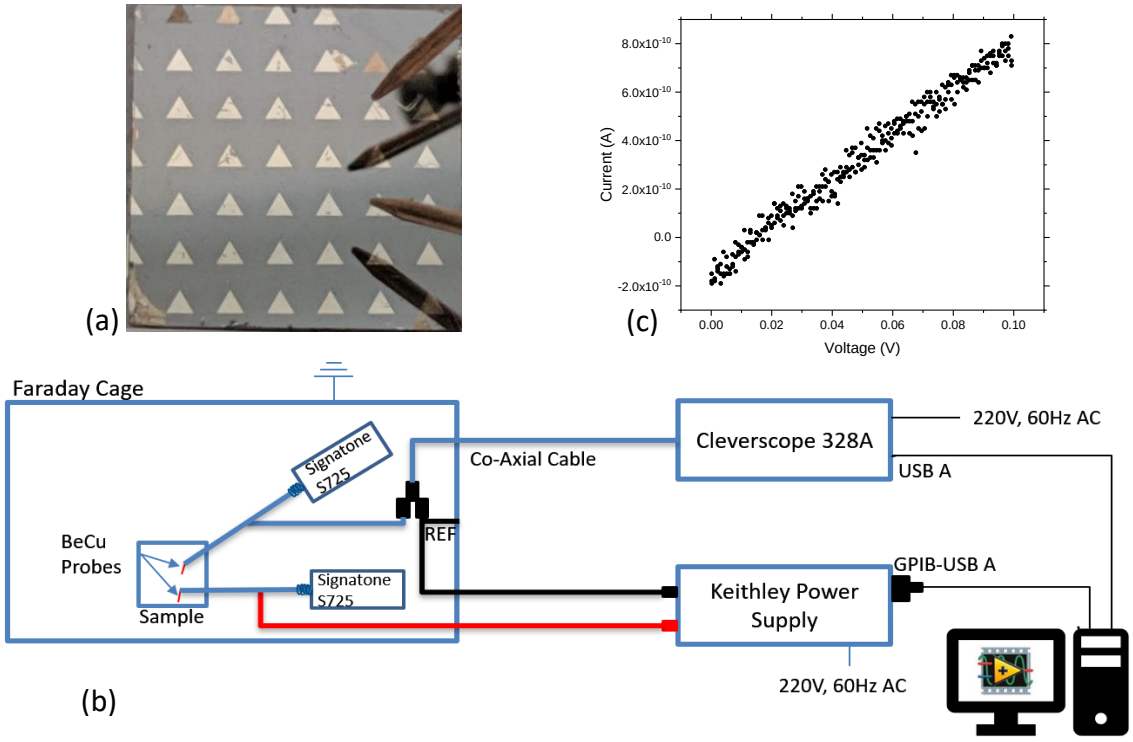

Figure A.1: (a) Image of sample with Al electrode contact points. (b) Diagram portraying the experimental setup for measuring currents in a sample. (c) 100MΩ Resistor baseline showcasing the nA resolution of the experimental setup

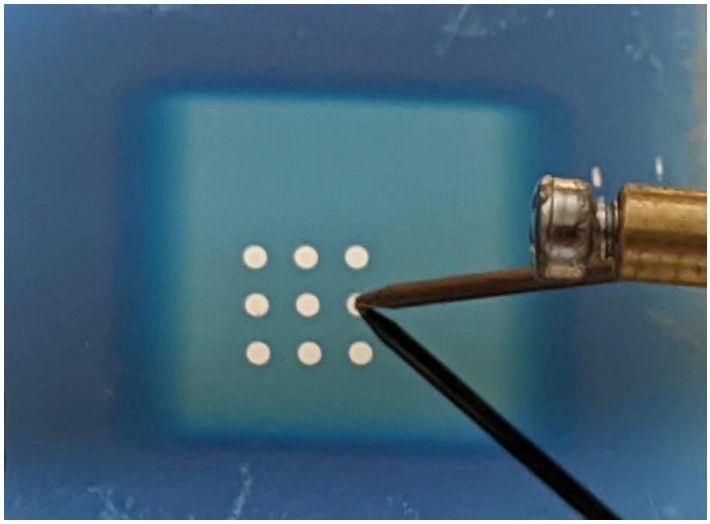

Figure A.2: Image of electrical probe on Al contact pad for an implanted sample (coloured region).

Appendix B – Chapter 3 Supplementary

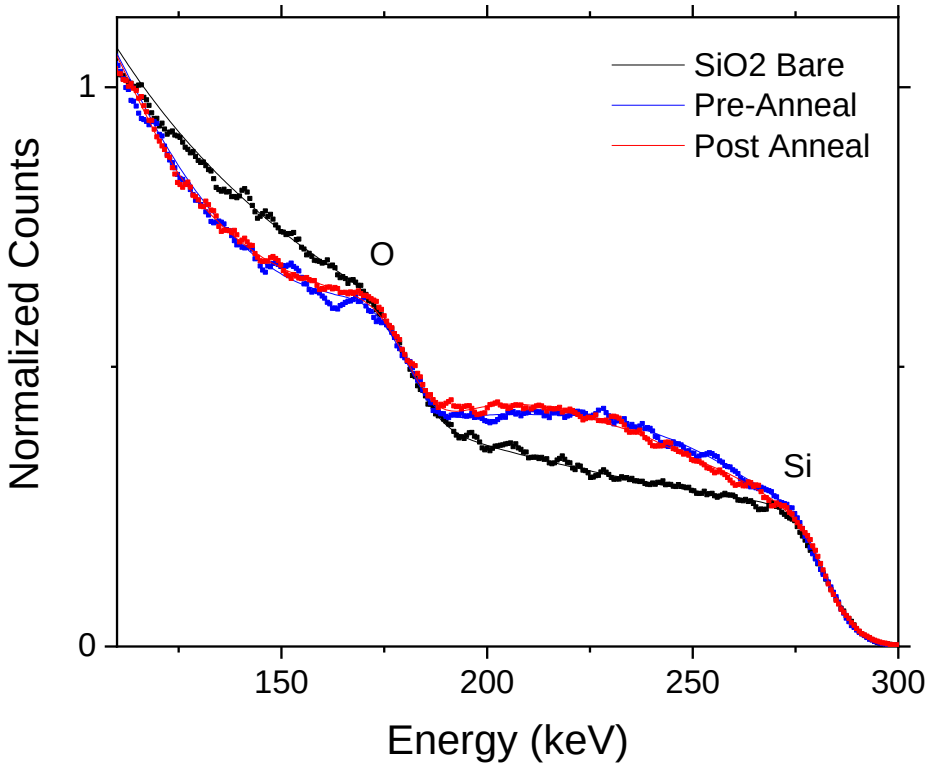

Figure B.1: RBS Spectra of Si implanted into SiO_2, both pre and post annealed, compared to bare SiO_2.

Appendix C – Chapter 4 Supplementary

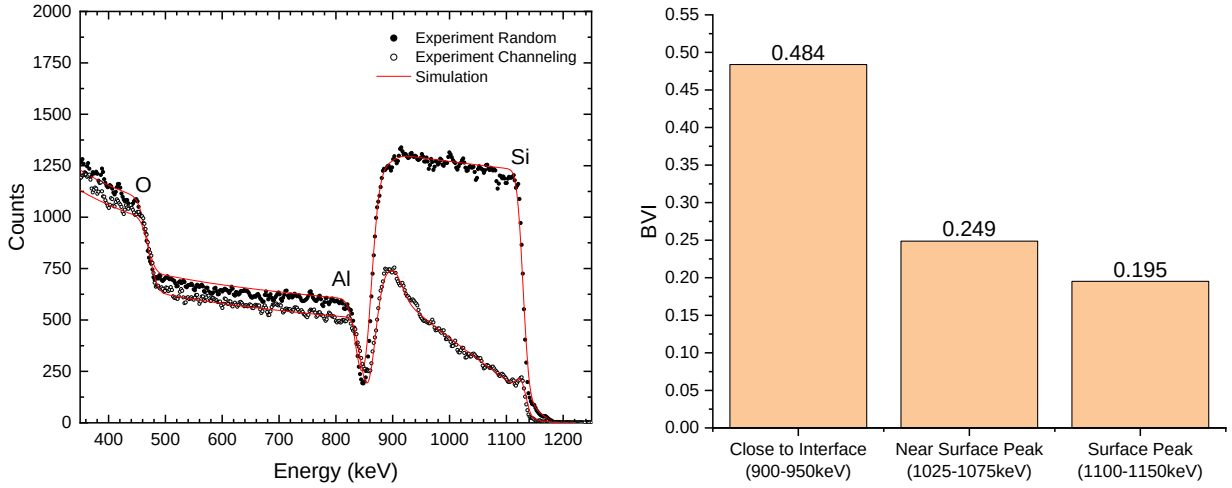

Figure C. 1: (a) RBS spectra of 0.6μm grown Si on sapphire taken at both random rotating and channeling angles. (b) BVI values showing an increase in defects closer to the interface.

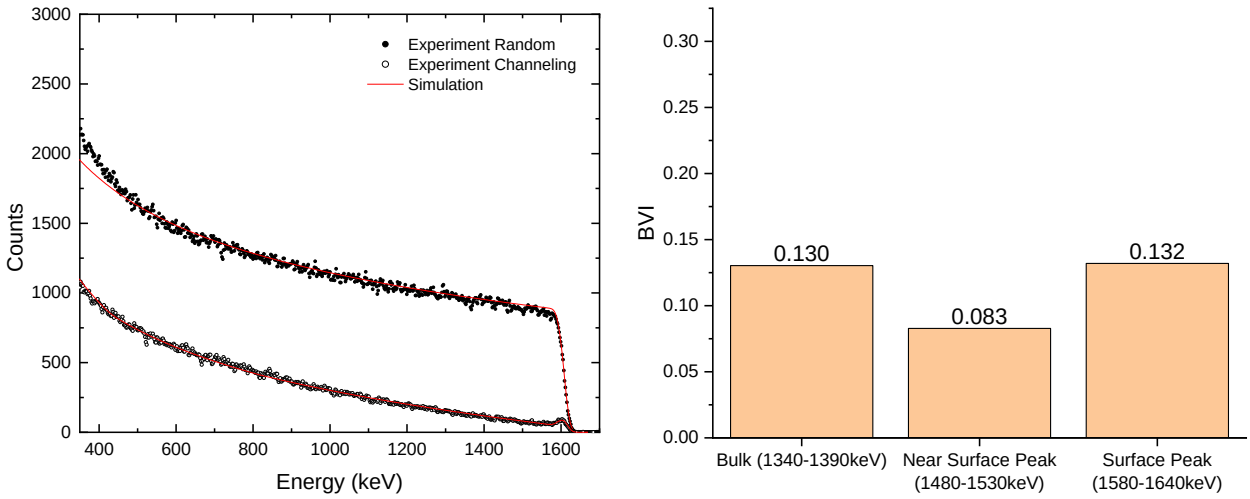

Figure C. 2: (a) RBS spectra of Ge(100) taken at both random rotating and channeling angles. (b) BVI values of Ge(100) showing an increase in defects at the surface.

Sample	Ratio Surface Peak (~0-5nm)	Ratio Near surface Peak	Ratio bulk, ~0.5um deep
Germanium	**1580-1640 keV**	**1480-1530 keV**	**1340-1390 keV**
Ge random	1.000	1.000	1.000
Ge (001) ch	0.132	0.083	0.130
Ge on Si (100)	0.136	0.168	0.285
Si100 (Silicon)	**1120-1175 keV**	**1025-1075 keV**	**Near Interface**
Si100 random	1.000	1.000	1.000
Si100 ch	0.068	0.039	0.046
SOS 0.6um random	1.000	1.000	1.000
SOS 0.6um ch	0.195	0.249	0.484
SOS 1.0um random	1.000	1.000	1.000
SOS 1.0um ch	0.102	0.127	0.527

Table C.1 Raw BVI values acquired through integrating RBS counts in the given ranges corresponding to different depth profiles and comparing normalized integral values to the random measurements. The lower the number, the fewer visible atoms (and corresponding defects in channeling) are present. It should be noted that numbers between different elements cannot be compared.

NAZBAN DARUKHANAWALLA

SKILLSET

- Nanomaterial Synthesis, Ion Implantation, Silicon Photonics
- Thin film Coating, Film Adhesion (Wetting), Cleanroom Experience
- FE-SEM, EDX, RBS, XPS, HF Etching, Lithography, Optical Bench Setup
- Python, Java, COMSOL, OriginPro, Numerical simulations
- Experience in presenting novel ideas to both internal and external customers
- Interdisciplinary background and problem-solving skills

EDUCATION

MSc University of Western Ontario, Physics December 2020

Thesis: "Fundamental transport properties in silicon quantum structures"

Abstract: "In the field of silicon photonics, there is an effort to bridge the gap between electrical and optical signals on a single platform, creating a need for Si-based light sources. In this project, Si quantum structures – Si quantum wells and quantum dots in SiO2 were fabricated via solid state precipitation methods. Their properties were studied using X-Ray Photoelectron Spectroscopy, photoluminescence and V-I measurements. Rutherford Backscattering Spectroscopy was used for depth analysis in monitoring the Si distribution. Different electrical transport mechanisms were explored to understand how an ensemble of silicon QD's or a silicon quantum well behaves in an SiO2 matrix, with conduction via oxide tunneling and hopping effects. Additionally, we quantified the defect density in epitaxially-grown Si and Ge thin films via RBS channeling, and correlated it with the Debye Temperature measured via low energy electron diffraction to assess the potential use of LEED as a technique for defect analysis."

Advisors: Dr. Lyudmila Goncharova & Dr. Peter Simpson

BSc University of Waterloo, Honors Physics & Astronomy December 2018
Co-op Education Program

HONORS AND AWARDS

Teaching Assistant Departmental Award 2020
Physics & Astronomy, University of Western Ontario

Graduate Research Award 2019
University of Western Ontario Research Bursary

Waterloo President's Scholarship 2013
University of Waterloo, Entry scholarship

PROFESSIONAL EXPERIENCE

Product Engineer Intern May 2017 to Dec 2017
Adaptive Surface Technologies, Harvard University
Location: Cambridge, MA, USA
Advisor: Philseok Kim

- Rapid optimization of novel hydrophobic coatings with FDA approval for a start-up linked to a Harvard lab
- Transitioned with the start-up from an R&D focus to a customer-based product with rapid upscaling of product line
- Created a cleanliness protocol for industrial hoppers that were to be spray-coated (HPLC, Air-Assist, Airless)
- Wrote python scripts automate data processing procedures, saving hours of work

Astronomy Researcher Jan 2016 to April 2016
NRC Herzberg Institute of Astrophysics
Location: Victoria, BC, Canada
Advisor: Patrick Cote & John Hutchings

- Worked with the Ultra-Violet Imaging Telescope (UVIT) onboard India's ASTROSAT space observatory
- Performance Verification of Spectral Filters in the UV-bandwidth
- Studied filters and detector performance
- Studied in-orbit performance of UVIT with first light images

Optical Engineer Intern Sep 2015 to Dec 2015
Christie Digital Systems Inc.
Location: Waterloo, ON, Canada
Advisor: Kennedy Landles (MEng.)

- High frequency pulsed lasers for novel laser projecting systems (20,000,000:1 contrast ratio, 30,000 lumens)
- Developed key components of an Android program for the characterization of fiber optic coatings
- Designed components of a RoHS compliant handheld microscope. Used alongside the android app to be in the field

Product Engineer Intern June 2014 to April 2015
Alchemy Inc. (Formerly Neverfrost Inc.)
Location: Waterloo, ON, Canada
Advisor: Chong Shen & Khanjan Desai

- Establishing foundational work in synthesis of **proprietary nanoparticles** used in an **anti- frost coating**
- Achieved particle size comparable to the **best in market** in just 4 months of development

- Work included various wet-lab synthesis, inorganic chemistry, polymer studies, nano-materials **characterization**
- Studied transmittance and reflectance of film composite through various wavelengths

TEACHING EXPERIENCE

University of Western Ontario, London Jan 2019 – April 2019
Teaching Assistant (First Year Physics), Department of Physics and Astronomy

- Oversaw and assisted students with their physics laboratory components
- Ran tutorials and taught 1st year physics in a lecture setting
    - Measurements, Electricity & Magnetism, Buoyancy
- Proctored examinations and graded papers

University of Western Ontario, London Sep 2019 - Current
Teaching Assistant (Intermediate Physics), Department of Physics and Astronomy

- Helped organize and ran both tutorials/labs and taught 2nd year physics.
    - Thermal Physics, Statistical Mechanics, Electromagnetism
- Proctored examinations and graded papers

PUBLICATIONS

Subramaniam, Annapurni, Snehalata Sahu, Joseph E. Postma, Patrick Côté, J.B. Hutchings, N. Darukhanawalla, S.N. Tandon, N. Kameswara Rao, K. George, S.K. Ghosh, V. Girish, R. Mohan, J. Murthy, A.K. Pati, K. Sankarasubramanian, C.S. Stalin, S. Choudhury. "The Horizontal Branch Population of NGC 1851 as Revealed by the Ultraviolet Imaging Telescope (UVIT)." The Astronomical Journal 154.6 (2017): 233. Crossref. Web.

PROFESSIONAL TRAINING

Science Communications Workshop, University of Western Ontario, September 2019
Description: Learning to improve upon presentation skills.

Project Management Workshop, University of Western Ontario, January 2019
Description: Learning about Project Management and its application to a professional degree

WHMIS Certification, University of Western Ontario, January 2019
Description: Workplace Hazardous Materials Information System. Required certification for laboratory work.

Laser Safety Certification, University of Western Ontario, January 2019
Description: Laser Safety designation. Understanding the different classes of lasers and warning labels associated with them.

Radiation Safety Certification, University of Western Ontario, January 2019

Description: Required to obtain government approved safety personal counters that are monitored twice a year.

EXTRACURRICULARS

Physics and Astronomy Graduate Council, Coordinator
University of Western Ontario, May 2019-Dec 2020

- Organizing social events (Potlucks, board games, ping pong tournaments)
- Attended the Society of Graduate Students Council meetings to vote on issues affecting graduate students

Waterloo Space Society, President
University of Waterloo, Jan 2014-Dec 2018

- Organizing Stargazing events, guest lecture and other social events with an attendance of around 40-200 students
- Pre-release screenings for a TIFF (Toronto Intl. Film Festival) movie
- Helped promotion for the NASA Space Apps Challenge/Hackathon
- Creating the backbone for multiple events such as model rocketry and flight simulation

Dubai Intl. Academy Space Agency, Founder & President
Dubai International Academy, Nov 2011 – May 2013

- Trained students in basic spaceflight and foundational university level physics. Brought over 30 students in exhibits promoting spaceflight and research
- Created the framework for future school clubs to be created and run by students

Perimeter Institute BrainSTEM Festival, Exhibit Presenter
Perimeter Institute for Theoretical Physics, October 2013

- Showcased and explained the basic features of various phenomenon such as Motion and Vibration Amplification, Wireless Electricity and Quantum Dots